Title: Integrated platform for multi-scale molecular imaging and phenotyping of the human brain

Authors: Juhyuk Park[1,2,3,15,†], Ji Wang[1,3,†], Webster Guan[2,†], Lars A. Gjesteby[7], Dylan Pollack[7], Lee Kamentsky[1,3], Nicholas B. Evans[1,3], Jeff Stirman[14], Xinyi Gu[5], Chuanxi Zhao[3], Slayton Marx[3], Minyoung E. Kim[4], Seo Woo Choi[2], Michael Snyder[7], David Chavez[7], Clover Su-Arcaro[3], Yuxuan Tian[2], Chang Sin Park[8,9], Qiangge Zhang[6], Dae Hee Yun[4], Mira Moukheiber[3], Guoping Feng[4,6], X. William Yang[8,9], C. Dirk Keene[12], Patrick R. Hof[13], Satrajit S. Ghosh[4,6,10], Matthew P. Frosch[11], Laura J. Brattain[7], and Kwanghun Chung[1,2,3,4,*]

Affiliations:

[1]Institute for Medical Engineering and Science, Massachusetts Institute of Technology (MIT), Cambridge, MA 02139, USA

[2]Department of Chemical Engineering, MIT, Cambridge, MA 02139, USA

[3]Picower Institute for Learning and Memory, MIT, Cambridge, MA 02139, USA

[4]Department of Brain and Cognitive Sciences, MIT, Cambridge, MA 02139, USA

[5]Department of Electrical Engineering and Computer Science, MIT, Cambridge, MA 02139, USA

[6]McGovern Institute for Brain Research, MIT, Cambridge, MA 02139, USA

[7]MIT Lincoln Laboratory, Lexington, MA 02421, USA

[8]Department of Psychiatry and Biobehavioral Sciences, David Geffen School of Medicine at UCLA, Los Angeles, CA, USA.

[9]Center for Neurobehavioral Genetics, Jane and Terry Semel Institute for Neuroscience, University of California, Los Angeles, CA, USA.

[10]Department of Otolaryngology, Harvard Medical School, Boston, MA 02114, USA

[11]C.S. Kubik Laboratory for Neuropathology, Massachusetts General Hospital and Harvard Medical School, Boston, MA 02114, USA

[12]Department of Laboratory Medicine and Pathology, University of Washington School of Medicine, Seattle, WA 98115, USA

[13]Nash Family Department of Neuroscience, Ronald M. Loeb Center for Alzheimer's Disease, and Friedman Brain Institute, Icahn School of Medicine at Mount Sinai, New York, NY 10029, USA

[14]LifeCanvas Technologies, Cambridge, MA 02141, USA

[15]Center for Nanomedicine, Institute for Basic Science, Seoul 03722, Republic of Korea

†These authors contributed equally to this work.

*Corresponding author. Email: khchung@mit.edu

Abstract: A detailed understanding of the anatomical and molecular architectures of cells and their system-wide connectivity is essential for interrogating system function and dysfunction. Extensive efforts have been made toward characterizing cells through various approaches, and have established invaluable databases yielding new insights. However, we still lack technologies for mapping the combined multi-scale anatomical and molecular details of individual cells in the human organ-scale system. To address this challenge, we developed a fully integrated technology platform for simultaneously extracting spatial, molecular, morphological, and connectivity information of individual cells from the same human brain at single-fiber resolution. We accomplished this by seamlessly integrating new chemical, mechanical, and computational tools to enable 3D multi-scale proteomic reconstruction of human organ tissues. We developed a novel microtome, termed MEGAtome, that enables ultra-precision slicing of whole-mount intact human brain hemispheres and large arrays of organs from other species with no loss of intra- and inter-slice cellular connectivity. To preserve structural and molecular information within intact human brain slabs and to enable multiplexed multiscale imaging, we developed a tissue-gel technology, termed mELAST, that transforms human brain tissues into an elastic and reversibly expandable tissue-hydrogel. To reconstruct the 3D connectivity of axonal networks across multiple brain slabs, we developed a computational pipeline termed UNSLICE. Using the technology platform, we analyzed Alzheimer's disease (AD) pathology at multiple scales from overall cytoarchitecture to individual synapses. Finally, we demonstrated the feasibility of scalable neural connectivity mapping in human brain, establishing a path for probing brain connectivity and its alterations in diseases.

One-Sentence Summary: We developed an integrated scalable platform for highly multiplexed multi-scale phenotyping and connectivity mapping in the same human brain tissue, which includes novel tissue processing, labeling, imaging, and computational reconstruction technologies.

Main Text:

A detailed mapping of the anatomical and molecular architectures of brain cells and their brain-wide connectivity is essential to understand human brain function and etiology and impact of brain injury and disease (*1–3*). Neuroimaging techniques (e.g., MRI, fMRI, DWI) have vastly increased our knowledge of the functional and structural organization of the human brain (*4–8*), but these methods fail to capture fine structural, cellular, and molecular details due to the limitations in spatial resolution (*9*, *10*). Advanced histological approaches have provided a new window into local organization of cells, but fail to capture brainwide 3D spatial information. Indeed, most histological studies resort to a subsampling approach, in which serial sections are stained for different markers, and coexpression analyses are limited by the host of the antibodies and the number of channels available for imaging.

With the development of high-throughput single-cell/single-nucleus RNA-seq technology (*3*, *11*), many more cell types can now be distinguished by their transcriptomic profiles, but these methods inherently limit the acquisition of spatial information and anatomical details of cells. Advances in spatial transcriptomics have enabled systematic analysis of the cellular composition within tissue context (*12*). Although these tools have dramatically advanced our understanding of the local cellular landscape of the brain, scaling these approaches to whole human brains across many individuals remains challenging. Moreover, transcriptomic analysis alone cannot provide key information critical to understand functional properties of cells, such as cellular morphology, connectivity, subcellular architectures, and posttranslational protein modifications.

Recently, much progress has been made in combining information across modalities. A study by the Allen Brain Institute for Brain Science in 2016, mapped the entire human brain using 50 µm-thick slices by alternating staining for Nissl, non-phosphorylated neurofilament protein, and parvalbumin, and combined this information with anatomical MR images of the same brain (*13*). This brain atlas was the first to integrate neuroimaging data with cyto- and chemoarchitectural data, thereby resulting in more thorough parcellations of brain regions and cells, as well as a comprehensive quantification of the complex interplay of microstructural features such as myeloarchitecture, cytoarchitecture, and vasculature in the human brain. However, we still lack scalable technologies that allow us to capture multi-scale multi-omic properties of individual cells and their brain-wide connectivity.

To address this challenge, we developed a fully integrated scalable technology platform for establishing a three-dimensional (3D) human brain cell atlas at subcellular resolution by simultaneously mapping brain-wide structure and high-dimensional features (e.g., spatial, molecular, morphological, microenvironment, nanoscopic and connectivity information) of cells

acquired from the same whole brains (**Fig. 1**). We accomplished this by seamlessly integrating new chemical, mechanical, imaging, and computational tools to enable highly multiplexed multi-scale 3D proteomic phenotyping of human brain tissues. We demonstrated its utility and scalability by processing whole human brain hemispheres and investigating Alzheimer's disease (AD) pathology.

MEGAtome enables high-precision slicing of ultra-large tissues

Mechanical tissue slicing is a crucial step for a wide range of biomedical applications despite recent progress in intact tissue clearing, labeling, and imaging technologies. State-of-the-art tissue clearing methods can render intact tissues, as large as rodent organs, optically transparent and chemically permeable. Cleared tissues can then be uniformly stained and rapidly imaged using high-speed microscopes equipped with long working distance (WD) objectives. However, molecular imaging of human and large animal organs still requires mechanical sectioning because the WD of available objectives cannot cover the entire tissue volume. Moreover, imaging up to the WD of even low NA (numerical aperture) objectives remains challenging due to loss of resolution caused by residual variations in refractive index within cleared tissues. These WD and loss of resolution limitations further restrict imageable tissue depth to only a few hundred microns when high resolution imaging with short WD and high NA objectives is required to resolve subcellular to nanoscopic features. Due to these fundamental challenges, mechanical tissue sectioning remains a crucial step for a broad range of biomedical studies.

Vibratome is one of the most commonly used tools for sectioning soft tissues into slabs with various thicknesses. Biological tissues are generally too soft to be cut without being "pushed" or deformed by an advancing blade. To solve this issue, a microtome or a cryostat, two other options widely used for tissue sectioning, require hardening of the tissue by paraffin or plastic resin embedding, or sample freezing before slicing. The hardened tissue can be sectioned as thin as several µm, but it is difficult to generate thick slices (> 200 µm), as thick and hardened tissue sections are prone to bend permanently during sectioning. A vibratome, on the other hand, can directly cut soft tissues into slices with a wide range of thickness thanks to its vibrating blade that applies oscillating shear cutting force to the sample. Because soft tissues are viscoelastic materials, their dynamic moduli increase as the vibrating blade exerts dynamic force on the material, leading the tissue to be "hardened" temporarily and locally by the vibration of the blade (*14*, *15*). This dynamically induced hardening enables slicing of soft tissues with any arbitrary thickness, covering a broad range of applications.

Conventional vibratomes, however, are limited to small samples and can cause tissue damage, leading to loss of crucial information. For example, one of the most commonly used commercial vibratomes has a maximum sample size of 33 mm [width] × 20 mm [height] × 50 mm [length]. Due to their limited blade vibrating speed and large out-of-plane blade vibration, cut surfaces suffer from abrasion, tear, and deformation. These damages cause loss of intra- and inter-slab information (e.g., tissue morphology, neural fiber connectivity). Commercial vibratomes also fail to uniformly slice highly inhomogeneous tissues, such as human brains, that have more significant anatomical complexity and inhomogeneity in tissue mechanical properties (e.g., meninges vs gray matter).

To address these limitations, we developed a highly versatile vibratome, termed MEGAtome (**M**echanically **E**nhanced **G**reat-size **A**brasion-free vibra**tome**), that enables ultra-precision slicing of a wide range of biological samples from small organoids (approximately 0.5 mm in diameter) to intact human brain hemispheres (approximately 65 mm [width] × 180 mm [height] × 130 mm [length]) and large arrays of animal organs (e.g., 35 mouse brains) with minimal loss of information (**Fig. 2**). MEGAtome minimizes tissue damage and maximally preserves intra- and inter-slice information by enabling high frequency blade vibration with large amplitude and low out-of-plane vibration displacement (**fig. S1**).

Analytical modeling and experimental observations have shown that the following three parameters together determine the precision and scalability of vibratome sectioning: (i) blade vibrating frequency, (ii) vibrating amplitude, and (iii) out-of-plane blade displacement (*16–18*). A vibrating blade exerts both shear force and normal force to a soft tissue during tissue slicing. The shear force, generated by blade vibration, plays the crucial role of “breaking” the tissue at the tissue-blade contact point by creating a critical stress and strain condition in the material. The normal force, generated by blade advancement into the material, assists the formation of the stress condition by pushing the material to deform. Material deformation, such as tissue stretching, caused mainly by the normal force is always preferred to be minimal in tissue slicing to prevent unwanted tissue damage. Analytical modeling and experimental observations have shown that, if the speed of the shear force is high, the critical “break” condition can be met with less normal force, meaning, intuitively, that a clean cut can be achieved by a rapidly vibrating blade (*16–18*). For the design of a vibratome, high blade vibrating frequency and amplitude, which are proportional to the speed of blade vibration, are desirable for slicing tissues with less tissue damage. In particular, high blade vibrating frequency is beneficial for slicing soft tissues because tissue shear deformation caused by the oscillating shear force decreases as its frequency increases. However, current commercial and custom vibratomes have limited blade vibrating

frequency and amplitude due to their inherent design trade-off between frequency and amplitude (*16, 19*).

The out-of-plane displacement of the blade, the distance that a blade moves away from its advancing plane, is another important factor that determines the quality of soft tissue slicing and its scalability to large samples. This unwanted blade movement causes tissue above and below the plane to be damaged by the blade, which worsens with increasing blade length. Minimizing out-of-plane displacement is therefore crucial for high precision slicing, but current commercial vibratomes suffer from high out-of-plane blade displacement, causing uneven slicing, which worsens as the tissue size increases, limiting their scalability to large samples (e.g., human brain and animal organ array).

To overcome these limitations, we developed a new blade vibration generation and control mechanism that can achieve high blade vibrating frequency, high amplitude, and minimal out-of-plane displacement all together (**Fig. 2, A, D, and E**). The system consists of a blade mounting assembly (BMA) that can secure a 120 mm-long custom-designed blade, three pairs of flexures (F_1, F_2 and F_3) that collectively act as a single-axis motion guide and a displacement amplifier for the blade mounting assembly, a voice coil actuator (VCA) that generates an oscillating force, and two laser displacement sensors (LDS) that measure the input and output vibration displacement (**Fig. 2D**). To operate the machine, a sinusoidal current is given to the moving coil of the VCA, which then generates an oscillating force to drive the blade mounting assembly to vibrate along the x-axis (**Fig. 2E**). The blade vibrating frequency and amplitude are controlled by the frequency and amplitude of the driving current. To control the feeding movement of samples as large as 115 mm [width] × 200 mm [height] × 300 mm [length], we designed a sample mounting and feeding platform (**Fig. 2, A and B**). The sample feeding speed is adjustable (0 - 50 mm/s) by controlling the speed of the motorized stage.

This multi-degree-of-freedom (multi-DOF) design (**Fig. 2F**, right) of MEGAtome can achieve high blade vibrating amplitude at high frequency unlike current commercial and custom vibratomes that are based on single-DOF system design (**Fig. 2F**, left) (*16, 19*). In single-DOF design, vibration input is directly applied to a blade mounting assembly (M) which is constrained by one spring component (K). Such system has an inherent design trade-off between its vibrating frequency and amplitude: a system with high spring stiffness can operate at a high frequency but low amplitude response; a system with low spring stiffness can achieve large amplitude but only at a lower frequency. On the other hand, MEGAtome's multi-DOF design is not subjected to the trade-off as its forced vibration response involves multiple design elements: two masses (M_1, M_2) and three springs (K_1, K_2, and K_3). The multi-DOF system can be modeled as a forced mass-

spring vibration system that consists of two moving masses (M_1, the intermediate mass connected to the VCA; M_2, the mass of the blade and the blade mounting assembly) and three springs (K_1, K_2, and K_3 representing their stiffnesses, respectively). A sinusoidal force is applied to the intermediate mass M_1 to indirectly drive the blade mounting assembly M_2. Simulation results of the single- and multi-DOF systems' forced response show that when given the same oscillating force, the multi-DOF system has two natural frequencies (~88 Hz and ~145 Hz), whereas the single-DOF system has one natural frequency (**Fig. 2G**). When excited near the natural frequencies, X_1 (vibrating amplitude of M_1) and X_2 (vibrating amplitude of M_2) are significantly increased due to mechanical resonance. Taking advantage of this property, we can drive the multi-DOF system near its higher natural frequency (~140 Hz) to generate increased blade vibrating. In comparison, the single-DOF system has one natural frequency at a much lower level (~70 Hz), and its amplitude drastically decreases if excitation frequency higher than 70 Hz is applied (**Fig. 2G**). Therefore, the operation of the single-DOF system is limited to lower frequency and lower amplitude.

To experimentally validate our computational model, we measured the vibrating amplitude, X_1 and X_2 of MEGAtome with the two laser displacement sensors (**Fig. 2, D and H**). Our results show that X_1 and X_2 are peaked at around 80 Hz (first resonant frequency) and 140 to 150 Hz (second resonant frequency), complying with the simulation results (**Fig. 2, G and H**). Considering that the blade vibrating speed u ($u = \dot{x_2}(t) = X_2\omega cos\omega t$) is the product of X_2 and the driving frequency ω, the maximum blade vibrating speed is realized at 140 Hz. We next measured vibration output amplitude versus vibration input amplitude for both MEGAtome and VT1200 at their optimal operating frequencies (**Fig. 2I**). Results show that MEGAtome's blade vibrating amplitude increases linearly with its vibration input and reaches 3.4 mm peak-peak value at 140 Hz, whereas VT1200 has its best performance at 2.4 mm peak-peak value and 85 Hz. Taken together, these results demonstrate that MEGAtome overcomes the trade-off between blade vibrating frequency and amplitude and realized 2.33 times higher blade vibrating speed than VT1200 at a 1.65 times higher frequency. Importantly, given that the output amplitude X_2 equals approximately 2.5 times of the input amplitude X_1 at the operating frequency, the mechanism realized vibration amplification with small excitation input, which is preferred because mechanical errors and noise caused by the actuator, such as actuator misalignment, can be reduced.

Minimizing blade out-of-plane parasitic vibration is critical to achieve precise and scalable tissue sectioning with minimal tissue damage. In the mechanical design of MEGAtome, we minimized this out-of-plane displacement by increasing the system's out-of-plane stiffness (**Fig. 2, D, E, and J**). The configuration of the flexures, particularly the vertical orientation of F_3, ensures

high stiffness in out-of-plane directions, including Z, θ_x and θ_y direction. To characterize this experimentally, we used high-precision capacitance probes (CP) to measure the out-of-plane displacement of the same blade that is mounted onto both MEGAtome and VT1200. The data confirmed that the out-of-plane vibrating amplitude of MEGAtome is significantly lower than that of VT1200 even though MEGAtome operates at much higher frequency (**Fig. 2K**). Next, we compared tissue slicing performance of the two machines by slicing large human cerebellum tissues (36 x 45 x 20 mm) from the same brain into 1, 0.2, and 0.1 mm-thick sections (**Fig. 2L**). The surface profile of the 1 mm-thick sections were measured using an optical profilometer (see Supplementary Materials). The heat map and the photos of the sections show that MEGAtome can generate intact slices with great surface evenness without damaging the fine tissue architectures (see zoom-in photos in **Fig. 2L**). On the other hand, the single-DOF system not only generated highly uneven tissue sections, but also caused severe damage to the cerebellar gyri and sulcus structures (**Fig. 2L**).

Next, we demonstrated information-lossless slicing using both human and mouse brain tissues. First, a human spinal cord tissue was MEGAtome-sliced into 200-μm-thick slabs. The slabs were then SHIELD-cleared, stained with anti-NFH antibodies and imaged using a confocal microscope (**Fig. 2M**). The confocal images taken from the adjacent slabs showed matching patterns of cross-sections of neuronal fibers at the slicing interface (zoom-in images of **Fig. 2M**) at single fiber resolution, indicating that MEGAtome slicing caused no damage or loss of fiber connectivity information. Second, an intact mononucleotide repeat frameshift (MORF) mouse brain expressing V5 peptide in a subset of neurons was SHIELD-cleared and eFLASH-stained (*20*) with anti-V5 antibody (*21*). We imaged the labeled whole brain using a light-sheet microscope to collect pre-slicing images as the ground truth data. The brain was then MEGAtome-sliced, and the slabs were imaged again using the same light-sheet microscope (**Fig. 2N**). By simply reconnecting the images of the after-slicing slabs and comparing it to the pre-slicing ground truth, we found the morphology of the V5+ neurons remained intact after slicing. Connectivity of the dendritic fibers was also completely preserved at the slicing interface at microscopic scale (second row in **Fig. 2N**), showing that MEGAtome provides an ideal solution for slicing tissues while keeping them “intact” at the same time.

Whole-mount slicing and imaging of intact human brain hemispheres and large organ arrays from other species.

To image large samples, such as human organs, the sample needs to be mechanically sliced to create mm-thick slabs. In this process, minimizing the number of dissected tissue blocks can drastically reduce human labor, cost, and information-loss associated with sectioning, manual handling, and subsequent processing of the dissected tissues. For instance, whole mount sectioning of an entire human brain hemisphere into intact 4-mm-thick coronal slabs is highly desirable because it generates only 40-50 slabs, whereas slicing the same brain into cube-shaped tissue blocks with the equal thickness produces thousands of pieces that are difficult to track and process without substantial human labor and resources. No vibratomes available, however, can realize whole-mount precision slicing of human-organ scale tissues. The challenges lie in not only the large size of the human organs, but also their complicated structure and highly inhomogeneous material properties that small samples lack. For example, in the human brain, tough meninges are buried deep in the sulci and surrounded by delicate gray matter. It is required for the vibratome to cut through these areas without dragging meninges into the gray matter thus causing damage. The human brain also has large internal ventricles, around which materials are not well supported or constrained from deforming during slicing, thus adding to the challenge of precision slicing.

Despite these challenges, MEGAtome was able to slice a whole-mounted human brain hemisphere and generate continuous, uniform and intact 4 mm-thick coronal slabs in a highly scalable manner (**Fig. 3, A-C** and **movie S1**). To whole-mount the human brain hemisphere and secure it in place during repeated slicing, we first poured liquid gel around the hemisphere in a custom-designed container that has detachable walls (**Fig. 3A**). After the gel became solidified, the walls of the container were detached. The gel block was submerged in 4% formaldehyde solution for seven days until sufficient bonding was formed between the tissue and the gel, followed by washing in PBS solution. Finally, the hemisphere was mounted onto MEGAtome for slicing in the coronal position. Each slice took 7-10 minutes and it took only 8 hours to cut an entire hemisphere into 40 four mm-thick slabs. **Figure 3C** shows the 40 consecutive 4 mm-thick coronal blocks from a whole human brain hemisphere successfully sliced with MEGAtome.

To image the large human brain tissues, we developed multicolor Inverted Axially-Swept Light-Sheet Fluorescence Microscopes (IASLSFM, **Fig. 3D**) with the capacity to capture multi-scale data with objectives ranging from 2x to 25x at near isotropic resolution (**fig. S2** and **table S1**). For full human brain slab imaging at cellular resolution, a 2x/0.1NA objective provides long working distances up to ~12 mm of depth. Each microscope is equipped with a continuous wavelength, multicolor laser source which operates at 405, 488, 561, 647, and 785 nm wavelengths. Custom-designed microscope stages can accommodate tissue dimensions of up to

180 x 380 mm, enabling super-resolution imaging of the expanded whole human brain coronal hemi slab (**Fig. 4J-i**). With IASLSFM, we can achieve high axial resolution with near-isotropic voxel size as well as high speed line-scanning detection. The system equipped with a 16.7x/0.4NA objective (15x magnification) can also be used for imaging expanded tissues at single-axonal resolution (**Fig. 4J-iv**).

Using the IASLSFM system, we demonstrated high-throughput imaging of a whole human brain hemisphere at subcellular resolution (**Fig. 3, F and H** and **fig. S2**). **Figure 3E** shows a SHIELD-preserved and cleared 4 mm-thick intact human brain coronal slab (110 mm x 75 mm) that contains multiple cortices, thalamus, and hippocampus regions. After NeuN staining, we imaged the whole slab and the 35 mouse brain array with IASLSFM only within 6 hours and 4 hours, respectively, capturing the 3D distribution of NeuN+ neurons in large volumes at single-cell resolution (**Fig. 3F**). Using one IASLSFM system, the whole brain hemisphere volume can be imaged at single cell resolution approximately within 100 hours. Considering that the human brain is one of the most complicated and largest human organs, we believe MEGAtome and IASLSFM are suitable for whole-mount precision slicing and high-resolution imaging of other human organs.

MEGAtome and IASLSFM also enable highly scalable molecular imaging of cohort-scale animal organs. Large-scale studies have greatly increased the need for imaging arrays of animal tissues in a high-throughput and cost-effective manner. However, the current approaches rely on manual handling of individual samples in a piecemeal manner that not only limits the throughput, but also increases human labor, cost, and sample-to-sample variations. To address this challenge, we developed a device and protocol that can create MEGAtome-compatible high-density sample arrays for high-throughput parallel processing and imaging of a wide range of biological samples (**Fig. 3G** and **fig. S3**). To maximize the slicing and imaging efficiency, the device ensures that each sample is positioned in the same exact orientation with minimal spaces in between. After MEGAtome slicing, both mouse and marmoset brain arrays were SHIELD-preserved, cleared, stained with anti-NeuN antibodies, and then imaged using IASLSFM, demonstrating high-throughput imaging using our mechanical and optical system (**Fig. 3H**).

mELAST enables rapid, highly-multiplexed labeling and multi-scale imaging.

We developed an integrated pipeline for tissue processing, termed mELAST (**m**agnifiable **E**ntangled **L**ink-**A**ugmented **S**tretchable **T**issue-hydrogel) by combining SHIELD, ELAST, and MAP (**Fig. 4A**) (*22–24*). SHIELD controls diffusion-reaction kinetics of epoxide-based fixatives to yield homogeneous preservation of molecules and tissue architecture (**Fig. 4A**). Proteins can be permanently preserved in fully delipidated SHIELD-tissue during iterative staining, imaging, and

destaining cycles. After SHIELD treatment, mELAST transforms tissues into an elastic, thermochemically stable, and reversibly expandable tissue-hydrogel via *in-situ* polymerization and subsequent post-processing (**Fig. 4, A and B** and **figs. S4-S5**) (*23*, *24*). By engineering a synthetic polymer hydrogel with highly entangled and super-absorbent polymeric chains for hybridizing biological tissues (*25*), we were able to achieve 4.5-fold linear expansion in DI water while keeping the tissue-gel elastic, intact, and highly durable (**Fig. 4, B and C**). mELAST successfully preserved protein epitopes (**fig. S6** and **table S2**) and there was no loss of structural information during periodic compression or tissue expansion (**fig. S7**). Once mELAST processing was done, we photobleached mELAST samples to remove endogenous autofluorescence (e.g., lipofuscin). We built a human brain-scale tissue photobleaching device and established protocols that can uniformly photobleach tissue autofluorescence throughout the thick tissue-gel (**Fig. 4, A, D, and E**). We were able to drastically reduce tissue autofluorescence and achieve high SNR (signal-to-noise rate) data acquisition (**Fig. 4, F, J-L** and **fig. S8**). The universal mELAST platform can be used for other species and organs without further optimization (**figs. S4C** and **S9**).

To achieve rapid, uniform, and cost-effective immunostaining of mELAST tissue-gels, we developed a SWITCH-pumping method that controls reaction kinetics by SWITCH (*26*) during rapid probes delivery by physical thinning (*23*). A custom-designed, human-brain-scale pump device enables highly reproducible mechanical tissue thinning by the relative linear movement between a pump head and a flat-bottomed container that encloses mELAST-processed tissues and labeling solutions (**Fig. 4G**). The tissue pump accelerates antibody delivery by reducing the characteristic tissue thickness and creating convective flow inside nanoporous tissue-gel via cyclic mechanical compression (**Fig. 4G-H**). During the cyclic compression, we modulated antibody-antigen binding reactions using a SWITCH-staining buffer with a non-denaturing ionic detergent (**fig. S10A**) to prevent depletion of antibodies along the tissue surface and enhance antibody penetration. This SWITCH-mediated tissue pumping allowed us drastically to reduce the amount of antibodies required for staining large tissue volume while improving the staining uniformity even for high copy-number targets, such as parvalbumin (PV), neurofilament heavy chain (NFH), and phosphorylated neurofilament proteins (pNFP) (**Fig. 4I** and **fig. S10B**). Automated operation of the pumps of various sizes ensures reproducible and scalable tissue labeling (**fig. S11**).

mELAST together with SWITCH-pumping enables multiplexed multiscale molecular imaging of large human brain tissues (**Fig. 4, J-L**). Using the SWITCH-pumping strategy, within 12 hours, we achieved completely uniform primary staining of an mELAST-processed whole human brain coronal slab (5.8 cm x 4.2 cm x 2.5 mm) with nuclear dye (YOYO-1), anti-CR and

anti-SST antibodies without any signal gradients in both gray and white matter (**Fig. 4J, i-iii** and **movie S2**). After staining, the entire volume of the mELAST tissue was first imaged using IASLSFM with the 2x objective and regions of interest were re-imaged with the 16.7x/0.4NA objective to acquire multi-scale information from the same tissue (**Fig. 4J, iv** and **movie S3**). After each round of staining and imaging, tissue underwent complete antibody elution. The tissue was then re-stained with the next set of antibodies. The universal applicability of the SWITCH-pumping method enabled uniform staining with all antibodies under identical conditions without additional optimization. The unprecedented structural stability of the mELAST tissue-gel allowed the samples to withstand mechanical stresses (~60,000 cycles of 4-fold compression for ~700 hours) without tissue damage. After successfully completing 7 rounds of staining and imaging of the brain slab within 5 weeks, we coregistered the multi-round datasets at single cell resolution using an algorithm that enables nearly perfect co-registration of all nuclei from different imaging rounds (**Fig. 4K-L; Fig. 5C; figs. S12-13**). The resulting dataset shows 3D distribution patterns of 11 major neuronal and non-neuronal markers.

Comparative multi-scale interrogation of the human brain tissues reveals distinct multi-dimensional features.

We applied the technology pipeline for interrogating the molecular and structural details of human brains from two donors across multiple brain regions (**Figs. 5-6**): Donor 1 (non-demented control) was a 61-year-old female with no clinical evidence of neurological impairment and low levels of AD neuropathologic changes (ADNC). Donor 2 (AD dementia) was an 88-year-old female with clinically suspected and neuropathologically confirmed AD dementia. We sliced the two donor hemibrains using MEGAtome and obtained intact coronal slabs at the same neuroanatomical level to ensure we studied cerebral gyri (e.g., superior frontal gyrus [SFG], rostral gyrus [RoG], cingulate gyrus [CgG], gyrus rectus [ReG], orbital gyrus [OrG], and mid frontal gyrus [MFG]) in alignment. The slabs were SHIELD-cleared and stained with a nuclear dye (YOYO-1) and an anti-NeuN antibody. The nuclear marker, which was included in every round of staining, enables detection of all nuclei and was used for coregistration of multi-round datasets at the single-cell level, while the pan-neuronal marker NeuN facilitates cytoarchitectural parcellations. The stained brain slabs were imaged at single-cell resolution using the IASLSFM system equipped with the 2x objective (**Fig. 5A**). We used a custom-built algorithm to perform 3D-segmentation of brain subregions in the volumetric datasets (Supplementary Materials). The resulting segmentation channel was used for cell counting and density calculation for each segmented brain region (**Fig. 5B**). The NeuN+ cells from both slabs were automatically detected using a 3D cell phenotyping

algorithm (**table S3,** detection accuracy=95.1%) (*27*). In the entire cortex area within the slabs, 7,464,727 NeuN+ cells were detected in the non-demented control brain and 2,890,858 NeuN+ cells were detected in the AD case. The NeuN+ cell density was 46.5% lower in AD dementia than in the control brain ($13.0\times10^3/mm^3$ vs $24.3\times10^3/mm^3$). In the control donor, no significant regional differences were found in the NeuN+ cell density (ranging from 24.4 to $25.0\times10^3/mm^3$), whereas in AD, the NeuN+ cell density in CgG and OrG were lower than those in other regions.

To investigate further cellular and molecular changes in the regions with high neuronal loss, we performed multiplexed immunohistological imaging of the orbitofrontal cortex (OFC from OrG) (**table S4**). The OFC is large region of the frontal cortex that has received considerable attention due to its role in high-order cognition tasks such as decision-making (*28*). The connectivity of the OFC is known to be impaired in later stages of AD, suggesting that its dysfunction may contribute to many of the non-memory-related behavioral changes observed in this disorder (*29*, *30*). To better understand the cell type- and structure-specific changes in the OFC in AD, we processed the tissues from the AD and control brains using mELAST, and performed multi-round immunostaining (Round 2 - Round 9) and multi-scale imaging using the 2x, 16.7x, and 63x objectives. Neuronal subtype markers (parvalbumin [PV], calretinin [CR], neuropeptide-Y [NPY], somatostatin [SST]), glia subtype markers (ionized calcium-binding adaptor molecule 1 [Iba1] for microglia, glial fibrillary acidic protein [GFAP] for activated astrocytes, myelin basic protein [MBP] for oligodendrocytes), structural pan-axonal marker (phosphorylated neurofilament proteins, [pNFP]), pathogenic protein markers (beta amyloid [Aβ], phosphorylated (Ser214 and Thr212 residues) tau [pTau]), endothelial cell marker [CD31/PECAM-1], and synaptic markers (synapsin I/II [Syn I/II], postsynaptic density protein 95 [PSD-95]) were used for multiplexing to map key cellular, structural, and pathological molecules. The multi-channel datasets were coregistered at single-cell resolution (**Fig. 5, C and D**, **figs. S12 and S14**, and **movies S4-5**).

We found distinct distribution patterns of the pathogenic proteins, Aβ and pTau, in AD vs. control (**Fig. 5, C-E** and **movie S6**). In AD, Aβ+ senile plaques enveloping pTau+ neurofibrillary tangles were densely distributed across the entire cortical area. In contrast, in the non-demented control, Aβ+ plaques were selectively localized in layer III with very few pTau+ neurofibrillary tangles. The GFAP distribution pattern between the donors was also very different (**Fig. 5, C-E** and **movie S6**). While interlaminar astrocytes located at the pial surface extended their processes to layers III and IV in the control tissues, the density of interlaminar astrocytes in AD was significantly lower and displayed processes that descended only into the boundary of layers II and III (*31*). Since the interlaminar astrocytes play an important role in stabilizing the physical structure

of the brain, structural stability might be weakened in AD (*32*). Severe reactive astrogliosis, an abnormal increase in the number of astrocytes due to neuroinflammation, was also observed (*33*, *34*).

Next, we investigated how axonal projection patterns in the OFC are altered in AD (**Fig. 5F-G** and **fig. S15**) by characterizing pNFP+ fiber orientations. We found that there were large populations of pNFP+ fibers in the control tissue that were oriented parallel, orthogonally, and obliquely to the pial surface, while pNFP+ fibers in the AD tissue were primarily oriented orthogonally, which is consistent with previous findings regarding axonal orientation shift in AD tissue (*35*). In the control tissue, orthogonally oriented fibers were found in all cortical layers, while obliquely and parallel oriented fibers were primarily found in cortical layers I, III, IV, and V (**fig. S15**). In the AD tissue, all six cortical layers had similar distributions of orthogonally oriented fibers. This suggests that pNFP+ axonal orientation is significantly shifted in AD.

To study how spatial organization of different cell types is affected in AD, we measured the density of nuclei and each neuron subtype in each cortical layer (**Fig. 5H**; **tables S5-7**; **Fig. S16**). The nuclei density measurement showed that the total number of cells in AD is lower than in the non-demented low pathology control. CR+ (in layers I-III), PV+ (in layers III-V), and CR+/ PV+ (in layers I-III) interneurons showed significantly lower density in AD, indicating neurodegeneration and impaired calcium homeostasis as well as changes in calcium-binding protein expression (**Fig. 5H**; **tables S6-7**) (*36*, *37*). The density of Iba1+ microglia was higher (1.81 times on average) across all cortical layers in AD than in control (**Fig. 5, C, D, and H**).

Next, we investigated the interrelationship between various cell types and neurofibrillary tangles (NFTs), a hallmark of AD (**Fig. 5I** and **table S8**). NFTs are abnormal accumulations of hyperphosphorylated tau, neurofilaments, and other cytoskeleton proteins, that result in neuronal dysfunction and ultimately death (*35*, *38–40*). We used anti-pNFP antibodies to visualize phosphorylated epitopes on medium and heavy subunits of neurofilament proteins. Unlike the non-demented control, in which no pNFP+ cell bodies were found, a large number of pNFP+ cell-bodies were detected in AD (**Fig. 5, D and I** and **fig. S16**). The pNFP+ cells were highly concentrated in layers III and V (77.1%), the major pyramidal cell layers (**Fig. 5, D and I**). None of the pNFP+ cells co-expressed the interneuronal markers (PV, CR, NPY, and SST), confirming selective vulnerability of pyramidal neurons in AD (**Fig. 5, D and I** and **tables 6-7**) (*39*, *40*). Most (82.6%) NFTs-containing neurons were pNFP+ (pTau+/ pNFP+, 54.2%; pTau-/ pNFP+, 28.4%) and only 17.4% were pTau+/ pNFP- cells, implying that phosphorylation of neurofilament proteins and their accumulation in specific neuronal populations may precede perikaryal pTau aggregation (**Fig. 5, D and I** and **table S8**).

To investigate further whether subcellular architectures are differentially altered in AD and the non-demented control, we performed high-resolution imaging of layer III where Aβ plaques were highly expressed in both cases (**Fig. 6**). Most of the Aβ plaques in AD were neuritic, dense-core plaques known to be closely associated with neuronal and synaptic loss, whereas Aβ plaques in the non-demented control were largely diffuse forms (**Fig. 6, A and B** and **movie S7**) (*41*). In the control, the majority of Iba1+ microglia were in the highly-branched, ramified form (77.6%), but microglia in the reactive form were observed inside and around diffused Aβ plaques (22.4%) (**Fig. 6, A, B, and F**) (*42*). Alternatively, in AD, most microglia (79.6%) were reactive, and rod-shaped microglia, whose function and role remain unknown but which are observed in numerous pathological conditions, were exclusively identified in AD (12.2%), but not in the control (0%) (**Fig. 6, A, B, and F**) (*43*). The elongated body axis of all rod-shaped microglia found in the region of interest were oriented perpendicular to the pial surface (**Fig. S17**). The morphological details of the GFAP+ astrocytes in layer III are shown in **Fig. 6, A and C**. In the non-demented control, GFAP+ structures were mostly long, unbranched processes of interlaminar astrocytes located near the pial surface. In AD, we could not find such long GFAP+ processes. Instead, most GFAP+ cells were protoplasmic astrocytes in reactive form, with 31.9-fold higher density of protoplasmic astrocytes in AD vs. to control.

Dendrite morphology analysis of CR+ interneurons revealed differences in arborization patterns between AD and the non-demented control (**Fig. 6, D and G**) (*44*). While the majority of CR+ cells in the control showed a multipolar dendrite morphology with complex branching patterns (69.7%), bipolar/bitufted neurons with less branching were more numerous in the AD case (61.5%). Interestingly, some bipolar/bitufted CR+ neurons in AD were peculiarly shaped, where their cell bodies were in contact with each other at a very close distance between their soma (**Fig. 6D**).

In AD, pTau+/pNFP+ fibers were abundant, indicating accumulation of pTau in axons (**Fig. 6, A, H, and J**), whereas in the control, only few pretangles and neuropil threads were observed (**Fig. 6, A and E**). While pTau-/pNFP+ axons in the non-demented control were thin (thickness=1.94±0.64 μm) and largely myelinated, many of the pTau+/pNFP+ axons inside the Aβ plaques in AD were significantly swollen (3.89±2.00 μm) and demyelinated (**Fig. 6, H-K**) (*45*). In AD, MBP pixel density inside the Aβ plaques was 10-fold lower than that outside the plaques, where in the control, we observed only 38.8% reduction in MBP pixel density (71.3±6.9 outside the plaques vs 43.6±5.0 inside the plaques) (**Fig. 6I**) (*46, 47*).

Finally, to investigate whether synaptic structures are damaged in AD, we performed super-resolution imaging of the same tissue region in both AD and control (**Fig. 6, L and M**). The

multiplexed mELAST tissues were destained and restained for the 9th round with antibodies targeting Aβ, PSD-95 (a postsynaptic marker), and Syn I/II (a presynaptic marker) (**table S4**). The stained tissue was expanded 4.5x in water and imaged using the 63x 1.3NA objective (**Fig. 6L** and **movie S8**). We assessed synaptic density inside and outside the Aβ plaques. While the synaptic density within the diffused Aβ plaques was similar with that outside of the plaques in the control case, we found a 10-fold decrease in synapse density (Syn I/II) inside the neuritic Aβ plaques compared to that outside (**Fig. 6, L and M**) (*48*). Interestingly, the synapse density outside of the Aβ plaques in AD and the non-demented control were similar. Collectively, these results demonstrate that our technology pipeline enables extraction of pathological changes at multiple scales from the same clinical samples.

Scalable computational pipeline for single-axon level inter-slab registration for human brain connectivity mapping.

Mapping the 3D connectivity of neural fibers across mechanically sliced tissues requires a computational pipeline that can register multiple slabs to reconstruct the original tissue volume with single fiber accuracy. Previous methods for computational tissue reconstruction tend to work with thin, undeformed, and/or laterally small tissue sections (*49–52*) that are unscalable to large, heavily-processed whole human hemisphere slab-scale images. Other methods that have been shown to scale to large mammalian tissue have not achieved accurate reconstruction of dense immunolabeled neurites in human tissue at single-fiber resolution (*53*). As such, reconstructing thick tissue accurately at both axonal-resolution and at large scales has yet to be accomplished.

To address these challenges, we developed a computational pipeline termed **U**nification of **N**eighboring **S**liced-tissues via **L**inkage of **I**nterconnected **C**ut fiber **E**ndpoints (UNSLICE), which can accurately align anatomical features at the macro-scale, meso-scale (blood vessels), and micro-scale (axons) levels. Intensity-based (e.g., optimization of a normalized cross-correlation loss function) or feature-based registration methods (e.g., Harris corner detector (*26*)) used for more standard 2D image registration applications do not scale well to inter-slab registration of large, thick, highly-processed, and immunostained tissue. Thus, to achieve accurate inter-slab registration at the macro- and micro-scale, more relevant and reliable features are required. To this end, UNSLICE takes advantage of fluorescent labeling of vasculature to match blood vessel endpoints at the cut surface in order to define a smooth deformation field for intact tissue reconstruction. Blood vessels are ideal features to use for inter-slab registration due to their long-range continuity and connectivity, high signal-to-noise ratio staining profile from lectin

dyes, which is compatible with most tissue clearing protocols, as well as their dense and ubiquitous distribution throughout the brain. By ensuring vessel connectivity throughout consecutive tissue slabs, good macroscopic and mesoscopic alignment of the two slabs can be achieved.

To achieve true neural fiber-resolution registration and connectivity within dense fibers, a variety of fine landmarks are required throughout the tissue. By using our scalable tissue processing, staining, and imaging pipeline (**Fig. 7A**) capable of acquiring highly multiplexed data at neural fiber resolutions, we can use multiple fiber-labeled cell type markers to iteratively refine our inter-slab registration (**Fig. 7B**). In particular, by immunostaining our tissue with a selection of specific cell type (such as PV and GFAP) and neurofilament protein markers (such as NFH), we can ensure comprehensive connectivity throughout two cut slabs at an unprecedented level unachievable through genetic labeling or lower resolution imaging.

UNSLICE utilizes the following steps for registering any pair of consecutive tissue slabs at vessel resolution (**Fig. 7B**): [1] image pre-processing, [2] surface detection, [3] flattening of the tissue based on detected surfaces using UV mapping (*54*), which is able to preserve physical surface topology and local surface point distances (**fig. S18**), [4] identification of matching "anchor points", [5] surface vessel endpoint detection, segmentation, skeletonization (*55*), and then masking to isolate surface endpoints using the mask detected in step [2] (**fig. S19**). [6] feature matching of endpoints between the two surfaces (**fig. S19**), [7] thin plate spline deformation of the moving image to fuse the volumes, [8] additional annotation of endpoints in the newly transformed frame, [9] iteratively perform steps [7-8] on the warped images to get progressively better connectivity alignment between the two slabs. This semi-automated process can be used to attain good registration between consecutive tissue slabs at vasculature resolution. Furthermore, by applying this method to image channels containing axonal or neural fiber information, we can also fine-tune the vasculature-scale registration to restore connectivity of axons across sliced tissue slabs (**Fig. 8A**).

To demonstrate that UNSLICE is capable of achieving single capillary and axonal-scale inter-slab registration, we applied UNSLICE on two different types of sliced tissue datasets for which the original intact tissues had already been imaged (thus providing a "ground truth"): [1] genetically labeled PV-Cre MORF mouse hemisphere slabs stained with lectin for blood vessels (**Fig. 7C**), and [2] expanded mELAST human cortical tissue immunostained for vasculature and neurofilament-H (**Fig. 7D**). Vasculature features were used to achieve capillary-resolution registration, and the registration was further fine-tuned using PV-Cre neural processes in the MORF mouse brain tissue or using immunostained axons in the mELAST-processed human

tissue. We achieved seamless reconstruction of the PV-Cre neural fiber connectivity through the cut surfaces in the MORF mouse tissue (**Fig. 7C**), while also preserving macroscopic morphology (**Fig. 7C**, left panels) when compared to ground truth images (**movie S9**). UNSLICE is robust to varying tissue types, stains, objectives, and datasets, as we demonstrated that it can successfully restore connectivity of NFH+ axons in expanded mELAST human tissue (**Fig. 7D**), which are much denser than the sparsely labeled MORF dataset. We quantified the accuracy of inter-slab registration by sampling three subregions per dataset and manually identifying corresponding fiber endpoints based on the ground truth images. We quantified the error of UNSLICE by computing the distance between perfectly matched corresponding fiber endpoints in both the MORF and mELAST human datasets, finding that the average error of MORF PV-Cre neural process reconstruction was 1.29 μm, and the average error of human mELAST axonal reconstruction was 1.13 μm (**Fig. 7E**). Through these experiments, we confirmed the viability of UNSLICE to inter-slab registration at single-fiber resolution.

To demonstrate the feasibility of using UNSLICE towards large tissue reconstruction on the human brain scale, we UNSLICEd consecutive 1 mm-thick SHIELD-processed human brain hemisphere coronal slabs (**Fig. 7, F and G** and **movie S10**). By ensuring connectivity of vasculature endpoints at the cut surface, it was possible to seamlessly stitch the two slabs back together. The computational flattening step in UNSLICE was particularly useful in this much larger dataset (**fig. S18**), as the larger lateral area and non-standard shape of the slabs make it harder to be processed, mounted, and imaged in a completely flat manner – a challenge not faced in most other applications of inter-slab registration. Furthermore, by combining manually defined correspondences for warp initialization with automated vessel endpoint matching in an iterative and parallelized fashion, the user has flexibility in choosing the level of precision required for inter-slab registration. The successful UNSLICE-ing of human coronal hemisphere slabs demonstrates the scalability of our pipeline towards proteomic and projectomic analysis of large-scale human brain tissue.

Multicolor, large-volume axonal projectome mapping in the human brain cortex and pathological analysis.

Since vasculature is not sufficiently dense to achieve the single-axon resolution registration required for comprehensive projectome mapping and axon tracing, cell type markers that stain for fibers and neurites are needed. The vasculature deformation field is first used for macroscopic and vessel-resolution registration before the fiber endpoints of other cell type markers such as GFAP, PV, and NFH are used to refine the registration results at the fiber-scale (**Fig. 8A-E**) to

enable multi-color spatial colocalization of multiple slabs (**Fig. 8C** and **movie S11**). Because UNSLICE's topographic feature matching and outlier removal steps were designed to tolerate both false negatives and positives in fiber endpoint detection, the same vesselness filter, segmentation, and skeletonization steps can be used for automated fiber endpoint detection, even with endpoint detection F1 scores in the 85%-90% range (**fig. S19**). We demonstrated that UNSLICE can achieve macroscopic registration using blood vessels (**Fig. 8B**), and the registration can then be progressively fine-tuned by including the endpoints of more markers (**Fig. 8, D and E**). The connectivity of individual NFH+ axons through the cut section of the tissue sections became progressively more accurate as more landmarks from different cell type markers are added (**Fig. 8E**). The connectivity of sparse astrocytic GFAP+ fibers is also improved by this multi-stage registration approach (**Fig. 8D**). The mean error magnitude of NFH connectivity after the vasculature-based registration is 20.8 μm; after addition of GFAP and PV landmarks the mean error magnitude is 7.85 μm, and after the final addition of NFH landmarks the mean error magnitude decreases to 2.35 μm (**Fig. 8, E and F**). The distribution of X and Y NFH connectivity error also shrinks from a spread of 10 microns (in each lateral dimension) after lectin registration, to ~5 μm after PV/GFAP registration, and finally to ~1 μm after NFH registration (**Fig. 8F**).

Automated and semi-automated neuron tracing and segmentation algorithms have previously been developed to analyze high-resolution images of single neurons or sparsely labeled groups of neurons (*56–58*). These algorithms are optimized primarily for two types of tasks: [1] subcellular segmentation and tracing at the nanoscale in electron microscopy images, or [2] reconstruction of single neuron morphology in fluorescence microscopy images, enabling fine analysis of the dendritic arborization of genetically labeled single neurons. While these algorithms are suitable for tracing high resolution, high SNR, sparsely-labeled light microscopy images, to the best of our knowledge, there are no algorithms available that have shown high-accuracy axonal tracing in densely immunostained tissue volumes. Towards this end, we have developed a deep-learning axon segmentation and tracing algorithm based on the U-Net, but extended for 3D datasets (**Fig. 8I**) (*59*). To perform end-to-end centerline detection, the algorithm uses a centerline-Dice (clDice) loss function (*60, 61*), which allows us to incorporate parameter-free skeletonization directly into the optimization process.

The inter-slab registration and automated axon tracing algorithms enabled the reconstruction of three consecutive mELAST-processed AD human tissue blocks at vasculature resolution (**Fig. 8, G and H**) and seamless connection of pTau+ axons across cut surfaces (**Fig. 8J** and **movie S12**). Multiple pTau+ fibers that traverse the tissue slab seams were reconnected, segmented, and traced using our pipeline without truncations (**Fig. 8, J and K** and **fig. S20**). Our

pipeline enabled us to analyze the orientation of traced pTau+ fibers throughout the whole reconstructed volume, finding that the majority of fibers are oriented in the direction corresponding to azimuthal angle θ=30°-60° (with 0° corresponding to perfect alignment with the z-axis and 90° corresponding to perfect alignment with the x-y plane) and polar angle φ=-30° to 30°, corresponding to fibers aligned with the x axis (**Fig. 8, L and M**). We also estimated the approximate orientation of the cortical column and compared our fiber orientation results to it. Qualitatively, we see that the majority of pTau+ fibers are generally aligned parallel to the cortical column (**Fig. 8N**). Combined with our histological and imaging platforms, this shows that our computational pipeline of inter-slab registration and axon tracing is accurate, scalable, and capable of enabling large scale connectivity mapping of human brain tissues.

Discussion

In summary, we developed multiple novel technologies and seamlessly integrated them to establish a scalable platform that enables fully integrated anatomical and molecular phenotyping of cells in human-organ-scale tissues with unprecedented resolution and speed. As the first step in human brain-scale tissue processing, MEGAtome realizes precision slicing of ultra-large tissues with minimal loss of intra- and inter-slab information. The mechanical design of MEGAtome overcomes the trade-off between blade vibrating frequency and vibration amplitude that limits the performance of state-of-the-art machines. The flexure based multi-DOF system design amplifies blade vibrating speed at high frequency, and at the same time minimizes the blade mechanical errors that are detrimental to tissue slicing. The synergistic gel-embedding protocol and MEGAtome slicing facilitates high-throughput slicing and imaging of ultra-large-scale brain samples at multiple scales while preserving fiber connectivity information between slabs.

The exceptional mechanical and chemical stability of the integrated SHIELD-mELAST platform enables highly multiplexed multiscale imaging of the same tissues with negligible information loss. For the first time, our unique expandable and compressible tissue gel allowed acquisition and integration of spatial proteomic data providing protein expression, cellular morphology, neural projection pattern, and synapse distribution pattern information from the same brain tissues, a highly desirable feature when considering inter-individual variation. The tissue-gel can be permanently stored and reimaged. This re-probing capacity will enable adaptive and iterative characterization of cell types and disease markers, a unique feature that maximizes the utility of the rare and highly important human clinical tissues. The highly durable and reusable nature of the SHIELD-mELAST platform will also enable the resulting datasets to continuously

evolve beyond the scope of individual studies by allowing the community to jointly prove the processed tissues and continue to extract information from the same samples.

Multi-scale phenotyping of the two human brains (non-demented control and AD dementia) using the platform elucidated distinctive molecular and structural features of the nervous system that are impacted in AD. Cellular level imaging allowed quantitative analysis of various neuronal and non-neuronal cell subtypes throughout the intact coronal slabs. Subsellular resolution imaging of the same brain tissues captured dissimilarities in the morphological properties of the cells in areas where different types of Aβ plaques are concentrated. Super-resolution imaging of the same tissue regions revealed the altered 3D distribution pattern of synapses within and outside the plaques. The multi-scale imaging and comparative analysis uncovered apparent pathological features in the AD tissue, including neuronal loss (NeuN, CR, PV), tauopathy (pTau), β- amyloidosis (Aβ), astrogliosis (GFAP), microgliosis (Iba1), myelinopathy (MBP), axonopathy (pNFP), vasculopathy (CD31), and synaptopathy (Syn I/II, PSD-95) as shown in Figs. 5 and 6. In particular, pTau-associated axonal swelling and correlated severe axonopathy/demyelination and synapse loss in regions surrounded by neuritic Aβ plaques supports the findings of neuroimaging studies that the connectivity of OFC is damaged severely in late stage of AD (*30*).

Determining neural circuit connectivity at a cellular level can provide long-sought insight into the essential character of brain function and dysfunction. Yet, mapping cellular connectivity in the human brain remains impossible because the current powerful circuit interrogation techniques (e.g., viral labeling) are only applicable to experimental animals. We, for the first time, demonstrated reconstruction of inter-slab axonal connectivity at single-fiber resolution in human brain tissues by integrating MEGAtome, mELAST, and UNSLICE. The accuracy of reconstruction and tracing will continue to improve as we increase the dimensionality of the integrated 3D datasets by adding additional rounds of 3D fiber-resolution images. The comprehensive circuit mapping enabled by this technology platform will enable the identification of non-canonical connections for better understanding of human brain circuitry.

We envision that this scalable technology platform will allow researchers to interrogate statistically significant numbers of human organs to adequately cover the spectrum of human demographic diversity and individual variability. Such baseline characterization of cellular, subcellular, and nanoscopic features will provide an immediately useful reference frame for the research community to study disease-specific changes in cell composition, spatial distribution, and subcellular architectures, advancing our understanding of the human organ functions and disease mechanisms to spur development of new therapies.

Materials and Methods Summary

The postmortem human brain hemispheres were first embedded in a gel for mounting and sliced using MEGAtome. The slicing quality was estimated by measuring the surface roughness using a VR machine and the vibration frequency. The sliced human brain tissues were SHIELD-processed and/or hybridized with an mELAST polymer hydrogel for permanent protein preservation and transformation into elastic, expandable materials. The engineered human brain tissues were passively or actively (using a SWITCH-pumping method) immunostained with antibodies and dyes and imaged at multiple scales using a confocal microscope or IASLSFM with various magnification objectives after optical clearing. The staining, imaging, and destaining process was repeated multiple rounds for multiplexing images. The IASLSFM imaging data was stitched and post-processed, and subject to computational analyses including brain subregion segmentation, cell/synapse counting, morphological reconstruction/classification and analyses. The images from the sectioned and engineered tissues were reintegrated using UNSLICE based on the end-point detection and matching at single axonal accuracy. The stitching accuracy of blood vessels and axons in the UNSLICE'd images was evaluated, and the characteristics were analyzed through fiber tracing. Full materials and methods are available in Supplementary Materials.

References and Notes

1. B. B. Biswal, M. Mennes, X. N. Zuo, S. Gohel, C. Kelly, S. M. Smith, C. F. Beckmann, J. S. Adelstein, R. L. Buckner, S. Colcombe, A. M. Dogonowski, M. Ernst, D. Fair, M. Hampson, M. J. Hoptman, J. S. Hyde, V. J. Kiviniemi, R. Kötter, S. J. Li, C. P. Lin, M. J. Lowe, C. Mackay, D. J. Madden, K. H. Madsen, D. S. Margulies, H. S. Mayberg, K. McMahon, C. S. Monk, S. H. Mostofsky, B. J. Nagel, J. J. Pekar, S. J. Peltier, S. E. Petersen, V. Riedl, S. A. R. B. Rombouts, B. Rypma, B. L. Schlaggar, S. Schmidt, R. D. Seidler, G. J. Siegle, C. Sorg, G. J. Teng, J. Veijola, A. Villringer, M. Walter, L. Wang, X. C. Weng, S. Whitfield-Gabrieli, P. Williamson, C. Windischberger, Y. F. Zang, H. Y. Zhang, F. X. Castellanos, M. P. Milham, Toward discovery science of human brain function. *Proc Natl Acad Sci U S A*. **107**, 4734–4739 (2010).
2. D. S. Bassett, M. S. Gazzaniga, Understanding complexity in the human brain. *Trends Cogn Sci*. **15**, 200–209 (2011).
3. M. J. Hawrylycz, E. S. Lein, A. L. Guillozet-Bongaarts, E. H. Shen, L. Ng, J. A. Miller, L. N. van de Lagemaat, K. A. Smith, A. Ebbert, Z. L. Riley, C. Abajian, C. F. Beckmann, A. Bernard, D. Bertagnolli, A. F. Boe, P. M. Cartagena, M. Mallar Chakravarty, M. Chapin, J. Chong, R. A. Dalley, B. D. Daly, C. Dang, S. Datta, N. Dee, T. A. Dolbeare, V. Faber, D. Feng, D. R. Fowler, J. Goldy, B. W. Gregor, Z. Haradon, D. R. Haynor, J. G. Hohmann, S. Horvath, R. E. Howard, A. Jeromin, J. M. Jochim, M. Kinnunen, C. Lau, E. T. Lazarz, C. Lee, T. A. Lemon, L. Li, Y. Li, J. A. Morris, C. C. Overly, P. D. Parker, S. E. Parry, M. Reding, J. J. Royall, J. Schulkin, P. A. Sequeira, C. R. Slaughterbeck, S. C. Smith, A. J. Sodt, S. M. Sunkin, B. E. Swanson, M. P. Vawter, D. Williams, P. Wohnoutka, H. Ronald Zielke, D. H. Geschwind, P. R. Hof, S. M. Smith, C. Koch, S. G. N. Grant, A. R. Jones, An anatomically comprehensive atlas of the adult human brain transcriptome. *Nature 2012 489:7416*. **489**, 391–399 (2012).
4. P. Glover, R. Bowtell, MRI rides the wave. *Nature 2009 457:7232*. **457**, 971–972 (2009).
5. A. C. Evans, A. L. Janke, D. L. Collins, S. Baillet, Brain templates and atlases. *Neuroimage*. **62**, 911–922 (2012).
6. K. Amunts, M. J. Hawrylycz, D. C. van Essen, J. D. van Horn, N. Harel, J. B. Poline, F. de Martino, J. G. Bjaalie, G. Dehaene-Lambertz, S. Dehaene, P. Valdes-Sosa, B. Thirion, K. Zilles, S. L. Hill, M. B. Abrams, P. A. Tass, W. Vanduffel, A. C. Evans, S. B. Eickhoff, Interoperable atlases of the human brain. *Neuroimage*. **99**, 525–532 (2014).
7. B. Fischl, M. I. Sereno, R. B. H. Tootell, A. M. Dale, High-Resolution Intersubject Averaging and a Coordinate System for the Cortical Surface. *Hum. Brain Mapping*. **8**, 272–284 (1999).
8. B. Fischl, A. M. Dale, Measuring the thickness of the human cerebral cortex from magnetic resonance images. *Proc Natl Acad Sci U S A*. **97**, 11050–11055 (2000).

9. K. Amunts, K. Zilles, Architectonic Mapping of the Human Brain beyond Brodmann. *Neuron*. **88**, 1086–1107 (2015).
10. S. Caspers, S. B. Eickhoff, K. Zilles, K. Amunts, Microstructural grey matter parcellation and its relevance for connectome analyses. *Neuroimage*. **80**, 18–26 (2013).
11. J. A. Miller, S. L. Ding, S. M. Sunkin, K. A. Smith, L. Ng, A. Szafer, A. Ebbert, Z. L. Riley, J. J. Royall, K. Aiona, J. M. Arnold, C. Bennet, D. Bertagnolli, K. Brouner, S. Butler, S. Caldejon, A. Carey, C. Cuhaciyan, R. A. Dalley, N. Dee, T. A. Dolbeare, B. A. C. Facer, D. Feng, T. P. Fliss, G. Gee, J. Goldy, L. Gourley, B. W. Gregor, G. Gu, R. E. Howard, J. M. Jochim, C. L. Kuan, C. Lau, C. K. Lee, F. Lee, T. A. Lemon, P. Lesnar, B. McMurray, N. Mastan, N. Mosqueda, T. Naluai-Cecchini, N. K. Ngo, J. Nyhus, A. Oldre, E. Olson, J. Parente, P. D. Parker, S. E. Parry, A. Stevens, M. Pletikos, M. Reding, K. Roll, D. Sandman, M. Sarreal, S. Shapouri, N. v. Shapovalova, E. H. Shen, N. Sjoquist, C. R. Slaughterbeck, M. Smith, A. J. Sodt, D. Williams, L. Zöllei, B. Fischl, M. B. Gerstein, D. H. Geschwind, I. A. Glass, M. J. Hawrylycz, R. F. Hevner, H. Huang, A. R. Jones, J. A. Knowles, P. Levitt, J. W. Phillips, N. Šestan, P. Wohnoutka, C. Dang, A. Bernard, J. G. Hohmann, E. S. Lein, Transcriptional landscape of the prenatal human brain. *Nature 2014 508:7495*. **508**, 199–206 (2014).
12. K. H. Chen, A. N. Boettiger, J. R. Moffitt, S. Wang, X. Zhuang, Spatially resolved, highly multiplexed RNA profiling in single cells. *Science (1979)*. **348** (2015), doi:10.1126/SCIENCE.AAA6090/SUPPL_FILE/CHEN-SM.PDF.
13. S. L. Ding, J. J. Royall, S. M. Sunkin, L. Ng, B. A. C. Facer, P. Lesnar, A. Guillozet-Bongaarts, B. McMurray, A. Szafer, T. A. Dolbeare, A. Stevens, L. Tirrell, T. Benner, S. Caldejon, R. A. Dalley, N. Dee, C. Lau, J. Nyhus, M. Reding, Z. L. Riley, D. Sandman, E. Shen, A. van der Kouwe, A. Varjabedian, M. Write, L. Zollei, C. Dang, J. A. Knowles, C. Koch, J. W. Phillips, N. Sestan, P. Wohnoutka, H. R. Zielke, J. G. Hohmann, A. R. Jones, A. Bernard, M. J. Hawrylycz, P. R. Hof, B. Fischl, E. S. Lein, Comprehensive cellular-resolution atlas of the adult human brain. *Journal of Comparative Neurology*. **524**, 3127–3481 (2016).
14. W. Li, D. E. T. Shepherd, D. M. Espino, Dynamic mechanical characterization and viscoelastic modeling of bovine brain tissue. *J Mech Behav Biomed Mater*. **114**, 104204 (2021).
15. B. Rashid, M. Destrade, M. D. Gilchrist, Mechanical characterization of brain tissue in compression at dynamic strain rates. *J Mech Behav Biomed Mater*. **10**, 23–38 (2012).
16. J. Wang, C. Li, S. C. Chen, Sectioning soft materials with an oscillating blade. *Precis Eng*. **56**, 96–100 (2019).
17. S. Mora, Y. Pomeau, Cutting and Slicing Weak Solids. *Phys Rev Lett*. **125**, 038002 (2020).
18. E. Reyssat, T. Tallinen, M. le Merrer, L. Mahadevan, Slicing softly with shear. *Phys Rev Lett*. **109**, 244301 (2012).
19. T. Jiang, B. Long, H. Gong, T. Xu, X. Li, Z. Duan, A. Li, L. Deng, Q. Zhong, X. Peng, J. Yuan, A platform for efficient identification of molecular phenotypes of brain-wide neural circuits. *Scientific Reports 2017 7:1*. **7**, 1–12 (2017).
20. D. H. Yun, Y.-G. Park, J. H. Cho, L. Kamentsky, N. B. Evans, A. Albanese, K. Xie, J. Swaney, C. H. Sohn, Y. Tian, Q. Zhang, G. Drummond, W. Guan, N. DiNapoli, H. Choi, H.-Y. Jung, L. Ruelas, G. Feng, K. Chung, Ultrafast immunostaining of organ-scale tissues for scalable proteomic phenotyping. *bioRxiv*, 660373 (2019).
21. M. B. Veldman, C. S. Park, C. M. Eyermann, J. Y. Zhang, E. Zuniga-Sanchez, A. A. Hirano, T. L. Daigle, N. N. Foster, M. Zhu, P. Langfelder, I. A. Lopez, N. C. Brecha, S. L. Zipursky, H. Zeng, H. W. Dong, X. W. Yang, Brainwide Genetic Sparse Cell Labeling to Illuminate the Morphology of Neurons and Glia with Cre-Dependent MORF Mice. *Neuron*. **108**, 111-127.e6 (2020).
22. Y. G. Park, C. H. Sohn, R. Chen, M. McCue, D. H. Yun, G. T. Drummond, T. Ku, N. B. Evans, H. C. Oak, W. Trieu, H. Choi, X. Jin, V. Lilascharoen, J. Wang, M. C. Truttmann, H. W. Qi, H. L. Ploegh, T. R. Golub, S. C. Chen, M. P. Frosch, H. J. Kulik, B. K. Lim, K. Chung, Protection of tissue physicochemical properties using polyfunctional crosslinkers. *Nature Biotechnology 2018 37:1*. **37**, 73–83 (2018).
23. T. Ku, W. Guan, N. B. Evans, C. H. Sohn, A. Albanese, J. G. Kim, M. P. Frosch, K. Chung, Elasticizing tissues for reversible shape transformation and accelerated molecular labeling. *Nature Methods 2020 17:6*. **17**, 609–613 (2020).

24. T. Ku, J. Swaney, J. Y. Park, A. Albanese, E. Murray, J. Hun Cho, Y. G. Park, V. Mangena, J. Chen, K. Chung, Multiplexed and scalable super-resolution imaging of three-dimensional protein localization in size-adjustable tissues. *Nature Biotechnology 2016 34:9*. **34**, 973–981 (2016).
25. S. W. Choi, W. Guan, K. Chung, Basic principles of hydrogel-based tissue transformation technologies and their applications. *Cell*. **184**, 4115–4136 (2021).
26. E. Murray, J. H. Cho, D. Goodwin, T. Ku, J. Swaney, S. Y. Kim, H. Choi, Y. G. Park, J. Y. Park, A. Hubbert, M. McCue, S. Vassallo, N. Bakh, M. P. Frosch, V. J. Wedeen, H. S. Seung, K. Chung, Simple, Scalable Proteomic Imaging for High-Dimensional Profiling of Intact Systems. *Cell*. **163**, 1500–1514 (2015).
27. A. Albanese, J. M. Swaney, D. H. Yun, N. B. Evans, J. M. Antonucci, S. Velasco, C. H. Sohn, P. Arlotta, L. Gehrke, K. Chung, Multiscale 3D phenotyping of human cerebral organoids. *Scientific Reports 2021 10:1*. **10**, 1–17 (2020).
28. A. Bechara, H. Damasio, A. R. Damasio, Emotion, Decision Making and the Orbitofrontal Cortex. *Cerebral Cortex*. **10**, 295–307 (2000).
29. G. W. van Hoesen, J. Parvizi, C. C. Chu, Orbitofrontal Cortex Pathology in Alzheimer's Disease. *Cerebral Cortex*. **10**, 243–251 (2000).
30. S. Tekin, J. L. Cummings, Frontal–subcortical neuronal circuits and clinical neuropsychiatry: An update. *J Psychosom Res*. **53**, 647–654 (2002).
31. J. A. Colombo, B. Quinn, V. Puissant, Disruption of astroglial interlaminar processes in Alzheimer's disease. *Brain Res Bull*. **58**, 235–242 (2002).
32. F. Vasile, E. Dossi, N. Rouach, Human astrocytes: structure and functions in the healthy brain. *Brain Struct Funct*. **222**, 2017–2029 (2017).
33. E. Colombo, C. Farina, Astrocytes: Key Regulators of Neuroinflammation. *Trends Immunol*. **37**, 608–620 (2016).
34. J. E. Simpson, P. G. Ince, G. Lace, G. Forster, P. J. Shaw, F. Matthews, G. Savva, C. Brayne, S. B. Wharton, Astrocyte phenotype in relation to Alzheimer-type pathology in the ageing brain. *Neurobiol Aging*. **31**, 578–590 (2010).
35. E. Masliah, M. Mallory, L. Hansen, M. Alford, R. DeTeresa, R. Terry, An antibody against phosphorylated neurofilaments identifies a subset of damaged association axons in Alzheimer's disease. *Am J Pathol*. **142**, 871 (1993).
36. F. Zallo, E. Gardenal, A. Verkhratsky, J. J. Rodríguez, Loss of calretinin and parvalbumin positive interneurones in the hippocampal CA1 of aged Alzheimer's disease mice. *Neurosci Lett*. **681**, 19–25 (2018).
37. J. B. Ruden, L. L. Dugan, C. Konradi, Parvalbumin interneuron vulnerability and brain disorders. *Neuropsychopharmacology 2020 46:2*. **46**, 279–287 (2020).
38. Q. Liu, F. Xie, S. L. Siedlak, A. Nunomura, K. Honda, P. I. Moreira, X. Zhua, M. A. Smith, G. Perry, Neurofilament proteins in neurodegenerative diseases. *Cellular and Molecular Life Sciences CMLS 2004 61:24*. **61**, 3057–3075 (2004).
39. T. Bussière, P. Giannakopoulos, C. Bouras, D. P. Perl, J. H. Morrison, P. R. Hof, Progressive degeneration of nonphosphorylated neurofilament protein-enriched pyramidal neurons predicts cognitive impairment in Alzheimer's disease: Stereologic analysis of prefrontal cortex area 9. *Journal of Comparative Neurology*. **463**, 281–302 (2003).
40. T. Bussière, G. Gold, E. Kövari, P. Giannakopoulos, C. Bouras, D. P. Perl, J. H. Morrison, P. R. Hof, Stereologic analysis of neurofibrillary tangle formation in prefrontal cortex area 9 in aging and Alzheimer's disease. *Neuroscience*. **117**, 577–592 (2003).
41. M. A. Deture, D. W. Dickson, The neuropathological diagnosis of Alzheimer's disease. *Molecular Neurodegeneration 2019 14:1*. **14**, 1–18 (2019).
42. P. T. Nelson, L. A. Soma, E. Lavi, Microglia in diseases of the central nervous system. *https://doi.org/10.1080/078538902321117698*. **34**, 491–500 (2009).
43. S. E. Taylor, C. Morganti-Kossmann, J. Lifshitz, J. M. Ziebell, Rod Microglia: A Morphological Definition. *PLoS One*. **9**, e97096 (2014).
44. G. A. Ascoli, L. Alonso-Nanclares, S. A. Anderson, G. Barrionuevo, R. Benavides-Piccione, A. Burkhalter, G. Buzsáki, B. Cauli, J. DeFelipe, A. Fairén, D. Feldmeyer, G. Fishell, Y. Fregnac, T. F. Freund, D. Gardner, E. P. Gardner, J. H. Goldberg, M. Helmstaedter, S. Hestrin, F. Karube, Z. F. Kisvárday, B. Lambolez, D. A. Lewis, O. Marin, H. Markram, A. Mũoz, A. Packer, C. C. H. Petersen, K. S. Rockland, J. Rossier, B. Rudy, P. Somogyi, J. F. Staiger, G. Tamas, A. M.

Thomson, M. Toledo-Rodriguez, Y. Wang, D. C. West, R. Yuste, Petilla terminology: nomenclature of features of GABAergic interneurons of the cerebral cortex. *Nature Reviews Neuroscience 2008 9:7*. **9**, 557–568 (2008).
45. A. Griffa, P. S. Baumann, J. P. Thiran, P. Hagmann, Structural connectomics in brain diseases. *Neuroimage*. **80**, 515–526 (2013).
46. X. Zhang, R. Wang, D. Hu, X. Sun, H. Fujioka, K. Lundberg, E. R. Chan, Q. Wang, R. Xu, M. E. Flanagan, A. A. Pieper, X. Qi, Oligodendroglial glycolytic stress triggers inflammasome activation and neuropathology in Alzheimer's disease. *Sci Adv*. **6** (2020), doi:10.1126/SCIADV.ABB8680/SUPPL_FILE/ABB8680_SM.PDF.
47. S. Mitew, M. T. K. Kirkcaldie, G. M. Halliday, C. E. Shepherd, J. C. Vickers, T. C. Dickson, Focal demyelination in Alzheimer's disease and transgenic mouse models. *Acta Neuropathol*. **119**, 567–577 (2010).
48. T. L. Spires-Jones, B. T. Hyman, The Intersection of Amyloid Beta and Tau at Synapses in Alzheimer's Disease. *Neuron*. **82**, 756–771 (2014).
49. S. Saalfeld, R. Fetter, A. Cardona, P. Tomancak, Elastic volume reconstruction from series of ultra-thin microscopy sections. *Nature Methods 2012 9:7*. **9**, 717–720 (2012).
50. A. Cardona, S. Saalfeld, J. Schindelin, I. Arganda-Carreras, S. Preibisch, M. Longair, P. Tomancak, V. Hartenstein, R. J. Douglas, TrakEM2 Software for Neural Circuit Reconstruction. *PLoS One*. **7**, e38011 (2012).
51. K. D. Micheva, S. J. Smith, Array Tomography: A New Tool for Imaging the Molecular Architecture and Ultrastructure of Neural Circuits. *Neuron*. **55**, 25–36 (2007).
52. S. Saalfeld, A. Cardona, V. Hartenstein, P. Tomančák, As-rigid-as-possible mosaicking and serial section registration of large ssTEM datasets. *Bioinformatics*. **26**, i57–i63 (2010).
53. F. Xu, Y. Shen, L. Ding, C. Y. Yang, H. Tan, H. Wang, Q. Zhu, R. Xu, F. Wu, Y. Xiao, C. Xu, Q. Li, P. Su, L. I. Zhang, H. W. Dong, R. Desimone, F. Xu, X. Hu, P. M. Lau, G. Q. Bi, High-throughput mapping of a whole rhesus monkey brain at micrometer resolution. *Nature Biotechnology 2021 39:12*. **39**, 1521–1528 (2021).
54. R. Sawhney, K. Crane, Boundary First Flattening. *ACM Transactions on Graphics (TOG)*. **37** (2017), doi:10.1145/3132705.
55. T. C. Lee, R. L. Kashyap, C. N. Chu, Building Skeleton Models via 3-D Medial Surface Axis Thinning Algorithms. *CVGIP: Graphical Models and Image Processing*. **56**, 462–478 (1994).
56. T. Quan, H. Zhou, J. Li, S. Li, A. Li, Y. Li, X. Lv, Q. Luo, H. Gong, S. Zeng, NeuroGPS-Tree: automatic reconstruction of large-scale neuronal populations with dense neurites. *Nature Methods 2016 13:1*. **13**, 51–54 (2015).
57. J. Winnubst, E. Bas, T. A. Ferreira, Z. Wu, M. N. Economo, P. Edson, B. J. Arthur, C. Bruns, K. Rokicki, D. Schauder, D. J. Olbris, S. D. Murphy, D. G. Ackerman, C. Arshadi, P. Baldwin, R. Blake, A. Elsayed, M. Hasan, D. Ramirez, B. dos Santos, M. Weldon, A. Zafar, J. T. Dudman, C. R. Gerfen, A. W. Hantman, W. Korff, S. M. Sternson, N. Spruston, K. Svoboda, J. Chandrashekar, Reconstruction of 1,000 Projection Neurons Reveals New Cell Types and Organization of Long-Range Connectivity in the Mouse Brain. *Cell*. **179**, 268-281.e13 (2019).
58. S. Banerjee, L. Magee, D. Wang, X. Li, B. X. Huo, J. Jayakumar, K. Matho, M. K. Lin, K. Ram, M. Sivaprakasam, J. Huang, Y. Wang, P. P. Mitra, Semantic segmentation of microscopic neuroanatomical data by combining topological priors with encoder–decoder deep networks. *Nature Machine Intelligence 2020 2:10*. **2**, 585–594 (2020).
59. O. Ronneberger, P. Fischer, T. Brox, U-Net: Convolutional Networks for Biomedical Image Segmentation. *ArXiv*. **1505** (2015), doi:10.48550/arxiv.1505.04597.
60. S. Shit, J. C. Paetzold, A. Sekuboyina, I. Ezhov, A. Unger, A. Zhylka, J. P. W. Pluim, U. Bauer, B. H. Menze, clDice -- a Novel Topology-Preserving Loss Function for Tubular Structure Segmentation. *Proceedings of the IEEE Computer Society Conference on Computer Vision and Pattern Recognition*, 16555–16564 (2020).
61. D. Pollack, L. A. Gjesteby, M. Snyder, D. Chavez, L. Kamentsky, K. Chung, L. J. Brattain, Axon Tracing and Centerline Detection using Topologically-Aware 3D U-Nets. *Annu Int Conf IEEE Eng Med Biol Soc*. **2022**, 238–242 (2022).
62. H.-E. Park, D. Choi, J. Su Park, C. Sim, S. Park, S. Kang, H. Yim, M. Lee, J. Kim, J. Pac, K. Rhee, J. Lee, Y. Lee, Y. Lee, S.-Y. Kim, H. Park, J. S. Park, C. Sim, H. Yim, M. Lee, J. Lee, S. Kim, J. Kim, K. Rhee, D. Choi, S. Park, S. Kang, J. Pac, Y. Lee, Y. J. Lee, Scalable and Isotropic

Expansion of Tissues with Simply Tunable Expansion Ratio. *Advanced Science*. **6**, 1901673 (2019).
63. G. Smets, A. M. Hesbain, Hydrolysis of polyacrylamide and acrylic acid–acrylamide copolymers. *Journal of Polymer Science*. **40**, 217–226 (1959).
64. Bourget, Microscopy-BIDS: an extension to the Brain Imaging Data Structure for Microscopy Data. *Front Neurosci* (2022).
65. J. Swaney, L. Kamentsky, N. B. Evans, K. Xie, Y.-G. Park, G. Drummond, D. H. Yun, K. Chung, Scalable image processing techniques for quantitative analysis of volumetric biological images from light-sheet microscopy. *bioRxiv*, 576595 (2019).
66. F. Piccinini, E. Lucarelli, A. Gherardi, A. Bevilacqua, Multi-image based method to correct vignetting effect in light microscopy images. *J Microsc*. **248**, 6–22 (2012).
67. K. J. Gorgolewski, T. Auer, V. D. Calhoun, R. C. Craddock, S. Das, E. P. Duff, G. Flandin, S. S. Ghosh, T. Glatard, Y. O. Halchenko, D. A. Handwerker, M. Hanke, D. Keator, X. Li, Z. Michael, C. Maumet, B. N. Nichols, T. E. Nichols, J. Pellman, J. B. Poline, A. Rokem, G. Schaefer, V. Sochat, W. Triplett, J. A. Turner, G. Varoquaux, R. A. Poldrack, The brain imaging data structure, a format for organizing and describing outputs of neuroimaging experiments. *Scientific Data 2016 3:1*. **3**, 1–9 (2016).
68. M. H. Bourget, L. Kamentsky, S. S. Ghosh, G. Mazzamuto, A. Lazari, C. J. Markiewicz, R. Oostenveld, G. Niso, Y. O. Halchenko, I. Lipp, S. Takerkart, P. J. Toussaint, A. R. Khan, G. Nilsonne, F. M. Castelli, J. Cohen-Adad, S. Appelhoff, R. Blair, E. Earl, F. Feingold, A. Galassi, R. Gau, T. Salo, Microscopy-BIDS: An Extension to the Brain Imaging Data Structure for Microscopy Data. *Front Neurosci*. **16**, 377 (2022).
69. J. Moore, C. Allan, S. Besson, J. M. Burel, E. Diel, D. Gault, K. Kozlowski, D. Lindner, M. Linkert, T. Manz, W. Moore, C. Pape, C. Tischer, J. R. Swedlow, OME-NGFF: a next-generation file format for expanding bioimaging data-access strategies. *Nature Methods 2021 18:12*. **18**, 1496–1498 (2021).
70. O. Rübel, A. Tritt, R. Ly, B. K. Dichter, S. Ghosh, L. Niu, P. Baker, I. Soltesz, L. Ng, K. Svoboda, L. Frank, K. E. Bouchard, The Neurodata Without Borders ecosystem for neurophysiological data science. *Elife*. **11** (2022), doi:10.7554/ELIFE.78362.
71. F. L. Bookstein, Principal Warps: Thin-Plate Splines and the Decomposition of Deformations. *IEEE Trans Pattern Anal Mach Intell*. **11**, 567–585 (1989).
72. Z. Püspöki, M. Storath, D. Sage, M. Unser, Transforms and operators for directional bioimage analysis: A survey. *Adv Anat Embryol Cell Biol*. **219**, 69–93 (2016).
73. Y. Wang, M. Eddison, G. Fleishman, M. Weigert, S. Xu, T. Wang, K. Rokicki, C. Goina, F. E. Henry, A. L. Lemire, U. Schmidt, H. Yang, K. Svoboda, E. W. Myers, S. Saalfeld, W. Korff, S. M. Sternson, P. W. Tillberg, EASI-FISH for thick tissue defines lateral hypothalamus spatio-molecular organization. *Cell*. **184**, 6361-6377.e24 (2021).
74. B. Appleton, H. Talbot, Globally minimal surfaces by continuous maximal flows. *IEEE Trans Pattern Anal Mach Intell*. **28**, 106–118 (2006).
75. W. K. Law, A. C. S. Chung, "Optimally oriented flux for curvilinear structure detection in volumetric images" in *10th European Conference on Computer Vision* (LNCS, Marseille, France, 2008; http://repository.ust.hk/ir/Record/1783.1-8338), pp. 368–382.
76. M. W. K. Law, A. C. S. Chung, An oriented flux symmetry based active contour model for three dimensional vessel segmentation. *Lecture Notes in Computer Science (including subseries Lecture Notes in Artificial Intelligence and Lecture Notes in Bioinformatics)*. **6313 LNCS**, 720–734 (2010).
77. H. W. Kuhn, The Hungarian method for the assignment problem. *Naval Research Logistics Quarterly*. **2**, 83–97 (1955).

Acknowledgments: We thank the entire Chung laboratory for support and discussions. Resources that may help enable general users to establish the methodology are freely available online (http://www.chunglabresources.org). The cartoon in Figure 1 was created with BioRender.com.

Funding: K.C. was supported by the Burroughs Wellcome Fund Career Awards at the Scientific Interface, Searle Scholars Program, Packard award in Science and Engineering, NARSAD Young Investigator Award, McKnight Foundation Technology Award. This work was supported by JPB Foundation (PIIF and PNDRF), NCSOFT Cultural Foundation, and NIH (1-DP2-ES027992, U01MH117072). J.P. was partially supported by the Institute for Basic Science (IBS-R026-D1). J.W. was supported by postdoctoral fellowships from the Picower Institute of Learning and Memory. W.G. was supported by the National Science Foundation Graduate Research Fellowship under Grant No. 1122374. M.P.F. was partially supported by NIA P50 AG005134. C.D.K. was partially supported by NIH P30 AG066509 and the Nancy and Buster Alvord endowment.

Author contributions: J.P., J.W., W.G., and K.C. conceived the idea and designed the experiments. J.P., J.W., W.G, and K.C. designed the platform and wrote the paper with input from other authors. J.P. developed mELAST technology and performed tissue processing, staining, and imaging of the brain tissues. J.W. developed MEGAtome and tissue-embedding method, and sliced the large-scale tissues. W.G. developed UNSLICE and performed inter-slab stitching of the images. N.B.E. and J.S. developed IASLSFM. L.K. developed the computational pipeline for processing IASLSFM images with help from M.M. L.K. developed co-registration of multi-round images. L.G., D.P., M.S., D.C., and L.J.B. developed the deep learning-based axon tracing algorithm and performed axon tracing on datasets with help from W.G. X.G. performed quantitative analysis of cells. C.Z. helped assemble machines and segmented the slab images. S.S.G. developed DANDI platform. S.M. and M.M. managed data storage. L.K. and S.S.G. were involved with standardizing the data. L.K., S.M., and S.S.G. curated, organized, and made available the data on DANDI. M.E.K. helped enhance image quality and performed synapses counting. W.G. stitched and post-processed IASLSFM images. J.W. developed tissue pumps and photobleachers. S.W.C. and J.P. developed slab-scale SHIELD-clearing protocol. J.P. coregistered multi-round images. J.P. screened and validated antibodies with help from D.H.Y. Y. T. prepared SeTau647-conjugated secondary antibodies. J.P. formulated the RI-matching media. C.S.-A. helped buffer preparation. C.S.P. and X.W.Y. provided MORF mouse brain samples. Q.Z. and G.F. provided marmoset brain samples. M.P.F. provided the human brain tissue specimens. M.P.F., C.D.K. and P.R.H. helped data interpretation. K.C. supervised all aspects of the work.

Competing interests: K.C. is a co-inventor on patent application owned by MIT covering the SHIELD and SWITCH technology (PCT/US2016/064538), the MAP technology (US Provisional Patent Application 62/330,018), and the ELAST technology (US Patent App. 17/308,462). K.C. and J. W. are co-inventors on patent application owned by MIT covering the MEGAtome technology. K.C. is a co-founder of LifeCanvas Technologies, a startup that provides solutions for 3D tissue processing and analysis.

Data and materials availability: In this study, the human brain microscopy image data from the SHIELD and mELAST tissues acquired using IASLSFM for the BICCN (RRID:SCR_015820) by Juhyuk Park and colleagues accessed/deposited in the DANDI Archive (RRID:SCR_017571) under accession number DANDI:000108. Data may be accessed at: https://dandiarchive.org/dandiset/000108/draft. The image data can be viewed immediately in neuroglancer from our lab's webserver (https://leviathan-chunglab.mit.edu/dandi/), to make that data viewable and analyzable by the scientific community. Direct access to the data on DANDI: https://biccn.github.io/Quarterly_Submission_Receipts/000108-dashboard.html. All other datasets used in this paper are available upon request. Code used for the paper can be found at the following Github repositories: https://github.com/chunglabmit/spimstitch (post-

acquisition pre-processing e.g., illumination correction, tile stitching, and file conversion), https://github.com/chunglabmit/unslice (UNSLICE), and https://github.com/chunglabmit/multiround-alignment-ui (multi-round image co-registration). The cell counting code will be released upon institutional review for open-source. The axon tracing code will be released upon institutional review for open-source.

Supplementary Materials

Materials and Methods

Figs. S1 to S20

Tables S1 to S8

References

Movies S1 to S12

Fig. 1. Integrated pipeline for multi-scale proteomic interrogation of the human brain. (**A**) The workflow of the pipeline for slicing, processing, labeling, imaging, and computational stitching of the human brain tissues. After MR imaging, human brain hemispheres are sliced into mm-thick coronal slabs using MEGAtome. The slabs are SHIELD-processed and transformed into mELAST tissue-hydrogels. The tough, elastic and size-adjustable mELAST tissue-gels are multi-round labeled and imaged at multiple scales to extract high dimensional features. The images acquired from the sliced human brain tissues are computationally reintegrated using the UNSLICE computational pipeline for multi-level connectivity mapping. (**B**) 3D multi-scale profiling of the human brain captures brain-wide structures, cytoarchitecture and local circuitry, cellular and subcellular features from the same tissue.

Fig. 2. Mechanical design and characterization of MEGAtome for scalable, information lossless slicing. (**A**) MEGAtome consists of two main modules: a blade vibration generation and control platform (in red frame), and a sample mounting and feeding platform (in blue frame). (**B**) The sample mounting and feeding platform is configured through two linear stages (LS). (**C**) MEGAtome can continuously and smoothly slice whole human brain hemispheres, and large arrays of mouse brains. (**D-E**) Mechanical design of the blade vibration generation and control mechanism shown in 3D view (D), and in XY plane (E). The mechanism mainly consists of 3 pairs of flexures (F_1, F_2, and F_3) and a blade mounting assembly (BMA). A voice coil actuator (VCA) drives the mechanism with oscillating force in x direction. Two laser displacement sensors (LDS) are used to measure the vibration input and output displacement. (**F**) Common commercial vibratomes (such as Leica VT1200) are designed based on the single degree of freedom (DOF) mass-spring vibration model (left), MEGAtome is designed based on a multi degree of freedom vibration model (right), in which K_1, K_2, K_3 represents the stiffnesses of F_1, F_2, and F_3, respectively. M_1 represents the mass where the driving force F is applied to, its displacement x_1 is measured by LDS1. M_2 represents the mass of the blade and blade mounting assembly, its displacement x_2 is measured by LDS2. (**G**) Simulation results of forced vibration response of a single DOF system, where blade vibration amplitude decays to minimal value as the driving frequency increases, and a multi DOF system, where high blade amplitude can be achieved at high frequency due to a second resonant mode. (**H**) Measurements of x_1 and x_2 show that the first and second resonant modes of the mechanism occur near 80 Hz and 140 Hz. (**I**) Measurements of blade vibration output versus vibration input of Leica VT1200 vibratome and MEGAtome. (**J**) Demonstration of ideal blade vibration and real blade vibration which is accompanied with parasitic errors. Three high-precision capacitance probes (CP) are used to measure blade parasitic vibration displacement. (**K**) Measurements of blade out-of-plane

parasitic vibration amplitude versus in-plane vibration amplitude of Leica VT1200 vibratome and MEGAtome. (**L**) MEGAtome generated 1-mm, 200-μm, and 100-μm slices from whole human cerebellums (top row). Leica VT1200 failed to generate complete slices at its maximum vibrating speed (bottom row). The 1 mm-thick slices were scanned by an optical profiler showing the surface height variance. Scale bars, 10 mm (whole slice figures) and 2 mm (enlarged figures). (**M**) MEGAtome do not cause loss of information in the cut area. NFH+ axons from the cut surfaces of the human brain spinal cord tissues maintain their location after MEGAtome slicing. (**N**) MEGAtome preserves neuron micromorphology and neural process connectivity while slicing. Neurons from PV-Cre MORF mouse brain tissues were imaged before and after MEGAtome slicing, and the shapes were compared. Top row scale bars, 500 μm; bottom row scale bar, 50 μm. The images were obtained with the 20x/0.5NA (M) and 4x/0.2NA objectives (N).

Fig. 3. Large-scale slicing and high-throughput imaging of the whole human brain hemisphere and array of organ-scale tissues. (**A**) Schematic drawing of whole mounting of intact human brain hemisphere for MEGAtome slicing. To gel-embed a whole human brain hemisphere, liquid gel is first poured onto the hemisphere in a custom-designed container that has detachable walls. After gel becomes solidified, walls of the container are detached. The gel is brought to be submerged in PFA solution. After sufficient fixation is formed between tissue and gel, the hemisphere is mounted onto the vibratome for slicing. (**B-C**) A banked human brain hemisphere was embedded in gel and then sliced by MEGAtome into 40 consecutive 4 mm-thick uniform slices that kept complete tissue from the hemisphere. (**D**) IASLSFM, a rapid, oblique-operated, and multicolor light sheet microscopy allows imaging of large-scale tissues. (**E**) High-throughput imaging of intact, volumetric human brain coronal slab. NeuN+ neurons were imaged in a 4 mm-thick SHIELD human brain coronal slab that contains multiple cortex regions, hippocampus, striatum and thalamus. (**F**) 3D image volume and enlarged xy plan views of NeuN+ cells from each brain region. (**G**) Custom-designed embedding tools allow for gel-embedding and vibratome slicing at least 35 brains (per area of 72 x 80 mm) together. (i) Gel-embedding process of mouse brain arrays starts with liquid gel being poured to the assembled tools. (ii) The mouse brain-shaped placeholders allow the gel to form fitted cavities to hold all brains in the same coronal position. (iii) More liquid gel is poured to immerse the brains fully. (iv) The solidified gel and brain mixture is fixed in PFA solution. (v) MEGAtome generates consecutive, uniform slices from an array. (**H**) MEGAtome in conjugation with IASLSFM allows for high-throughput imaging of neurons from the organ-arrays. Arrays of 35 mouse brains and 6 marmoset hemispheres were embedded and sliced together following the protocol in (G), SHIELD-cleared, stained with anti-NeuN antibodies, and imaged using IASLSFM. The images were obtained with the 2x/0.1NA objective (E, F, and H). Anatomical annotations in E from Allen Brain Reference Atlases (Adult Human, Modified Brodmann), http://atlas.brain-map.org (*13*).

Fig. 4. mELAST tissue processing and staining methods for multiplexed multi-scale molecular imaging of the thick human brain tissues. (**A-C**) mELAST technology transforms intact, slab-scale human brain tissues into a transparent, permeable, tough-elastic, and size-adjustable material. (**A**) The photos show the processing workflow of an intact human brain coronal slab. Scale bar, 2 cm. (**B**) mELAST human brain tissue-hydrogels are highly elastic and linearly 4-5x expandable in water. Scale bar, 1 cm. (**C**) Size-adjustability of PFA tissues and mELAST tissue-gels are compared in 1XPBS and water. L0 is the mean length of the original brain. L is the mean length in 1XPBS or water. (**D**) A photobleaching device removes autofluorescence from lipofuscin and other autofluorescence pigments in human brain tissue. (**E**) Mean background signal values of IASLSFM images before and after photobleaching are compared. Scale bar, 300 μm. (**F**) Photobleaching allows for high signal-to-noise imaging. Scale bar, 100 μm. (**G**) A large human-brain-scale tissue pump enables accelerated immunolabeling

of large-scale mELAST tissue-gels. An mELAST tissue-gel is placed in a chamber with buffer solution and repeatedly compressed for clearing, washing, staining, and destaining. (**H**) A graph measuring the distance between the pump head and the chamber floor when the pump operates. The inset graph shows the accuracy of the device with a very small error of the order of 10 μm. (**I**) SWITCH-pumping staining allows rapid, uniform, and cost-effective immunostaining of mELAST tissue-gels. Three same-sized mELAST human brain tissue-gels were stained with POPO-1 (nuclear dye), anti-PV, and anti-NFH antibodies using passive, pumping and SWITCH-pumping methods, and the staining uniformity was compared. Scale bar, 100 μm. (**J**) Multi-scale imaging of an mELAST-processed coronal human brain hemisphere tissue. The slab-scale mELAST tissue was SWITCH-pumping stained with YOYO-1 (nuclei dye), anti-CR, anti-SST antibodies and imaged using IASLSFM (2x [i, ii, iii] and 16.7x [iv]), capturing the slab-wide wiring [ii], spatial cell distribution [iii] and morphological detail [iv] of neurons within the same tissue. Scale bars, 1 cm [i], 2 mm [ii], 500 μm [iii], and 20 μm [iv]. (**K**) Highly multiplexed imaging of an mELAST human brain tissue. The mELAST cortex tissue was multi-round SWITCH-pumping stained and IASLSFM-imaged, and the images were computationally co-registered based on nuclei dye patterns included in each round. Scale bars, 2 mm. (**L**) Zoom-in view of the multiplexed image. Scale bars, 100 μm. The images were obtained with the 2x/0.1NA (E, J-i, ii, iii and K), 20x/0.5NA (F and I), and 16.7x/0.4NA objectives (J-iv).

Fig. 5. Comparative multi-scale imaging and multi-dimensional phenotyping of the human brains, Part 1: Single-cell level. (**A-B**) Intact coronal hemi-scale tissue processing and imaging allows for holistic quantitative analysis of individual cells in large tissue volumes. (**A**) Immunolabeled NeuN+ cells in intact coronal hemisphere slabs from the control and AD cases were imaged. (i) Cortical subregions in the whole slab images were segmented. The two slabs contain matching cortical areas. (ii) Enlarged view of orbitofrontal cortex (OFC from OrG). (iii) NeuN+ cells were detected using a generalist 3D cell phenotyping algorithm and automatically counted for each cortex subregion. (**B**) The graphs show the difference in the number and density of NeuN+ cells in each brain subregion. (**C-D**) Multiplexed staining and imaging of mELAST-processed human brain tissues from OFC of the non-demented control and AD slabs described in Fig. 5A allows for single-cell resolution multiplexed molecular cell phenotyping. The mELAST tissue-gels were subject to repeated SWITCH-pumping staining, destaining, and imaging using IASLSFM; nuclei (YOYO-1), neuronal subtypes (PV, CR, NPY, SST), astrocytes (GFAP), microglia (Iba1), oligodendrocyte (MBP), axons (pNFP), endothelial cells (CD31), senile plaques (Aβ), and neurofibril tangles (pTau). Scale bar, 200 μm. (**E**) Differing signal intensity profile of GFAP, Aβ, and pTau across the cortical column from the two cases. (**F-G**) pNFP+ cortical fiber orientation analysis. (**F**) Representative images show that pNFP+ fibers were oriented parallel, obliquely, and orthogonally to the pial surface throughout the cortex of the control tissue and oriented parallel, obliquely, and orthogonally to the pial surface throughout the cortex in the AD tissue (Yellow arrows represent the pial surface direction). (**G**) Histograms of pNFP+ neural fiber angular orientation with respect to cortical column direction (θ) in the full control and AD tissues. Blue peaks in the histogram (i) suggest large populations of fibers oriented parallel (0º,180º), orthogonally (90º), and obliquely (30º, 120º) to the pial surface in the control tissue. The orientation distribution varies somewhat between different cortical layers (fig. S16). Red peaks in the histogram (ii) suggest only one large population of fibers oriented orthogonally (90º) to the pial surface in the AD tissue. (**H**) Layer-specific comparison of the density and distribution of the (i) YOYO-1, (ii) PV+, CR+, NPY+, SST+, CR+/ PV+ neurons and (iii) Iba1+ microglia in the OFC of the control and AD. (**I**) Spatial distribution pattern of pTau and pNFP associated cells. Layer-specific comparison of (i) cell density and (ii) proportion of each subtype of pTau+/ pNFP -, pTau-/ pNFP+ and pTau+/ pNFP+ cells in each

layer. Scale bar, 100 μm. The images were obtained with the 2x/0.1NA objective (A, C, D, and F).

Fig. 6. Comparative multi-scale imaging and multi-dimensional phenotyping of the human brains, Part 2: Subcellular level. (**A**) Fine morphological details of the cells in the same, expanded mELAST tissue-gels described in Fig. 5, C and D. After each round of low-resolution imaging using the 2x objective, a region of interest, layer III was imaged again with the 16.7x/0.4NA objective. Scale bar, 50 μm. (**B**) Iba1+ microglia morphology. 3D rendering of each type of Iba1+ microglia in the control and AD. Most microglia in the control were in ramified form but clustered microglia in diffuse Aβ plaque were in reactive form. In AD, most microglia were in reactive form clustering close to neuritic plaques and many rod-shaped microglia were found, which were missing in the control. (**C**) GFAP+ astrocyte morphology. In AD compared to the control, an overwhelming number of reactive forms of GFAP+ astrocytes were found. (**D**) CR+ interneuron morphology. Most CR+ interneurons in the control were in a normal shape but some CR+ interneurons in AD appeared to be fused and they were mostly CR+/ PV+. (**E**) pTau+ cells and fibers morphology. In the control, only a couple of pTau+ pretangles were found in the entire image volume, whereas a countless mature tangles, neuropil thread and dystrophic neurites were found in AD. (**F**) Cell density of each glia type classified based on their morphology. (**G**) Percentages of CR+ interneurons in the control and AD cases classified by their dendrite morphology: bipolar, bitufted, multipolar (n=3), and multipolar (n>3). (**H-J**) Multi-scale imaging and analysis of axonal damage. (**H**) At single cell resolution, the pNFP+ axons in the neuritic plaques in AD were pTau+ and mostly demyelinated, whereas the axons in the diffuse plaques in AD were relatively unaffected without axon swelling. Scale bar, 50 μm. (**I**) MBP pixel density analysis shows the extent of demyelination in the non-demented control and AD inside and outside Aβ plaques. (**J**) pNFP+ axon and MBP+ oligodendrocyte morphology at subcellular level. Most axons in the control were covered with myelin sheath but many axons in AD, represented by the marked region in Fig. 6H were swollen and demyelinated. (**K**) Distribution of thickness of representative pNFP+ axons in the control and AD tissues. (**L**) 3D mapping of chemical synapses (Syn I/II and, PSD-95) and Aβ plaques in the same 4.5x expanded control and AD mELAST human brain tissue-gels described in Fig. 6A. Scale bars, 5 μm and 500 nm (zoom-in view). In AD, severe synapse loss was observed within the majority of neuritic plaques, particularly in Syn I/II, whereas in the control, there was no significant loss within the majority of diffuse plaques. (**M**) Comparison of the density of Syn I/II and PSD-95 in the control and AD, inside and outside Aβ plaques. The images were obtained with the 2x/0.1NA (H), 16.7x/0.4NA (A-E, and J), and 63x/1.2NA objectives (L).

Fig. 7. UNSLICE computational pipeline enables accurate, human-scale inter-slab registration to reconstruct sliced tissue blocks. (**A**) Projectome mapping of large intact tissue requires processing, staining, and imaging of sliced mm-thick slabs followed by computational reconstruction, axon tracing, and downstream analysis. (**B**) Macro-scale inter-slab registration pipeline (termed UNSLICE) at vasculature registration involves first flattening the surfaces, preliminarily aligning the slabs using manually selected anchor points, and then non rigid deformation based on feature matching between geographically similar vessel endpoints, performed iteratively for increasing levels of registration accuracy. (**C**) UNSLICE enables 3D reconstruction of genetically labeled PV+ neurons in MORF mouse brains, as verified by comparison to images of the tissue pre-slicing (ground truth). Scale bars, 500 μm (macroscopic view) and 50 μm (zoom-in views). (**D**) UNSLICE enables 3D reconstruction of sliced, expanded human mELAST-processed tissue at axon-scale resolution. Compared to the intact tissue imaged pre-slicing (ground truth), UNSLICEd images show restoration of axonal connectivity between slabs. Scale bars, 100 μm (macroscopic view) and 25 μm (zoom-in view). (**E**) Validation of UNSLICE evaluated by quantifying the distance (error) between fiber endpoints

at the cut surface in three sampled subsections based on ground-truth image data before and after slicing at cellular resolution (C, SHIELD mouse brain tissue; average error 1.29 μm) and subcellular resolution (D, expanded mELAST human brain tissue; average error 1.13 μm). (**F**) Inter-slab registration of two adjacent coronal human brain hemisphere slabs. Lectin channel of SHIELD-processed consecutive coronal human slabs (x-y and x-z optical cross sections). Scale bars, 2 mm. Pre-registration to post-registration maximum intensity projections (MIP) of x-y cross sections of coronal human slabs. Inset images show blood vessels connected across the cut surface. Scale bars, 2 mm. Preregistration to postregistration MIPs of x-z cross-sections. Inset zoomed-in section images show blood vessel continuity across slabs. (**G**) 3D rendering of the registered coronal human brain slabs. Scale bar, 5 mm. The images were obtained with the 2x/0.1NA (F-G), 4x/0.2NA (D), and 16.7x/0.4NA objectives (C).

Fig. 8. Multicolor subcellular resolution imaging and UNSLICE enable single-fiber resolution axon reconstruction and connectivity mapping in human cortical tissue. (**A**) Axon-level UNSLICEing is achieved by starting with the vasculature-registered slabs, and then using finer features such as astrocytic processes or neural axonal fibers to achieve progressively finer scale registration. (**B**) Using lectin, two cortical human tissue slabs were inter-slab-registered to single-vessel resolution, providing a groundwork for fine-tuning using the other neural fiber channels. Scale bars, 1 mm. (**C**) UNSLICE enables multi-channel reconstruction at axon resolution. Zoomed in section from (B) with overlay of GFAP, lectin, NFH, and PV showing multicolor reconstruction. Scale bars, 100 μm and 25 μm (zoomed-in images). (**D**) Demonstration of NFH and GFAP registration at single axonal fiber resolution within a single field of view of the larger cortical tissue. Scale bars, 100 μm. Inset images show xz and xy NFH and GFAP maximum intensity projections (MIP) of one field of view within the slabs. After using the coarse macroscale lectin registration parameters, NFH+ axons can nearly be connected through the slabs. NFH axonal fibers and astrocytic fibers can be easily connected by eye after registration using PV+ and GFAP+ fiber endpoints. NFH+ axons and GFAP+ fibers are nearly perfectly connected through consecutive tissue slabs after fine-tuning the registration with NFH endpoints. (**E**) Fibers in a small inset of the field of view can be progressively better connected using multi-channel registration. (**F**) (top) Histogram of absolute errors for NFH axonal fibers and (bottom) x-y lateral connectivity errors for NFH axonal fibers during each step of the registration process (vasculature registration, PV/GFAP fine-tuning, and NFH fine-tuning). (**G-N**) Synergizing UNSLICE with MEGAtome and mELAST technologies facilitates pTau fiber mapping and analysis in AD human brain cortex tissue. (**G**) mELAST processed and sliced AD human brain cortical tissue containing cortical layers IV and V can be reconstructed with UNSLICE, achieving macroscopic and vascular-scale accuracy registration. Scale bars, 0.5 mm. (**H**) The transformation field calculated using vasculature can be applied to the Aβ and pTau channels. Scale bars, 0.5 mm. Inset prisms: see subfigures (J and K). (**I**) Deep-learning based axon tracing algorithm performs end-to-end detection of axon centerlines by using a residual 3D U-Net architecture that directly utilizes centerline DICE score (clDICE) as loss function. (**J**) UNSLICE and axon tracing pipeline enables volumetric tracing of pTau fibers across cut tissue-slices. insets (i)-(iii): Zoomed in xz MIP overlaid with tracing results showing single pTau fiber tracing across tissue slices. Scale bars, 150 μm. (**K**) Aβ (red) / pTau (grayscale) overlay of the same subvolume from (J). insets (i)-(ii): Zoomed in subvolumes depicting two segmented long traced pTau fibers among Aβ plaques. Scale bars, 150 μm. (**L**) pTau fiber orientation histogram of traced fibers from the subvolume in (J), binned by polar angle (φ) and azimuthal angle (θ). The thickness of the vector was proportional to fiber counts in a given direction. Most pTau fibers in this tissue were oriented in the x direction (φ = [-30º,30º]) and the θ = [30º,60º] direction. (**M**) Histograms from (L) projected into the XY, XZ, and YZ planes. (**N**) Orientation of the majority of fibers was oriented parallel to the cortical column.

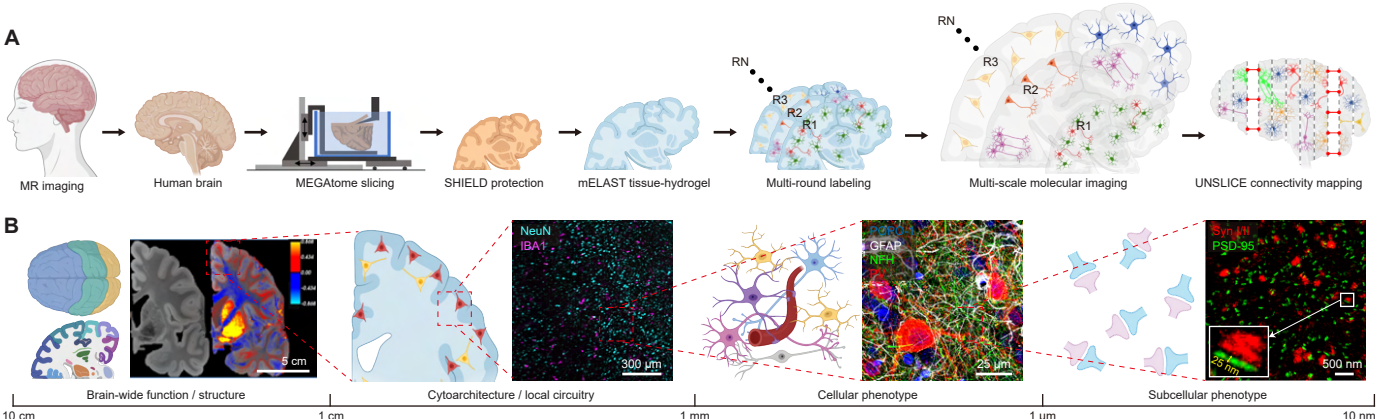
A
MR imaging
Human brain
MEGAtome slicing
SHIELD protection
mELAST tissue-hydrogel
RN
R3
R2
R1
Multi-round labeling
RN
R3
R2
R1
Multi-scale molecular imaging
UNSLICE connectivity mapping
B
5 cm
NeuN
IBA1
300 μm
GFAP
NeuN
25 μm
Syn I/II
PSD-95
25 nm
500 nm
Brain-wide function / structure
Cytoarchitecture / local circuitry
Cellular phenotype
Subcellular phenotype
10 cm
1 cm
1 mm
1 μm
10 nm

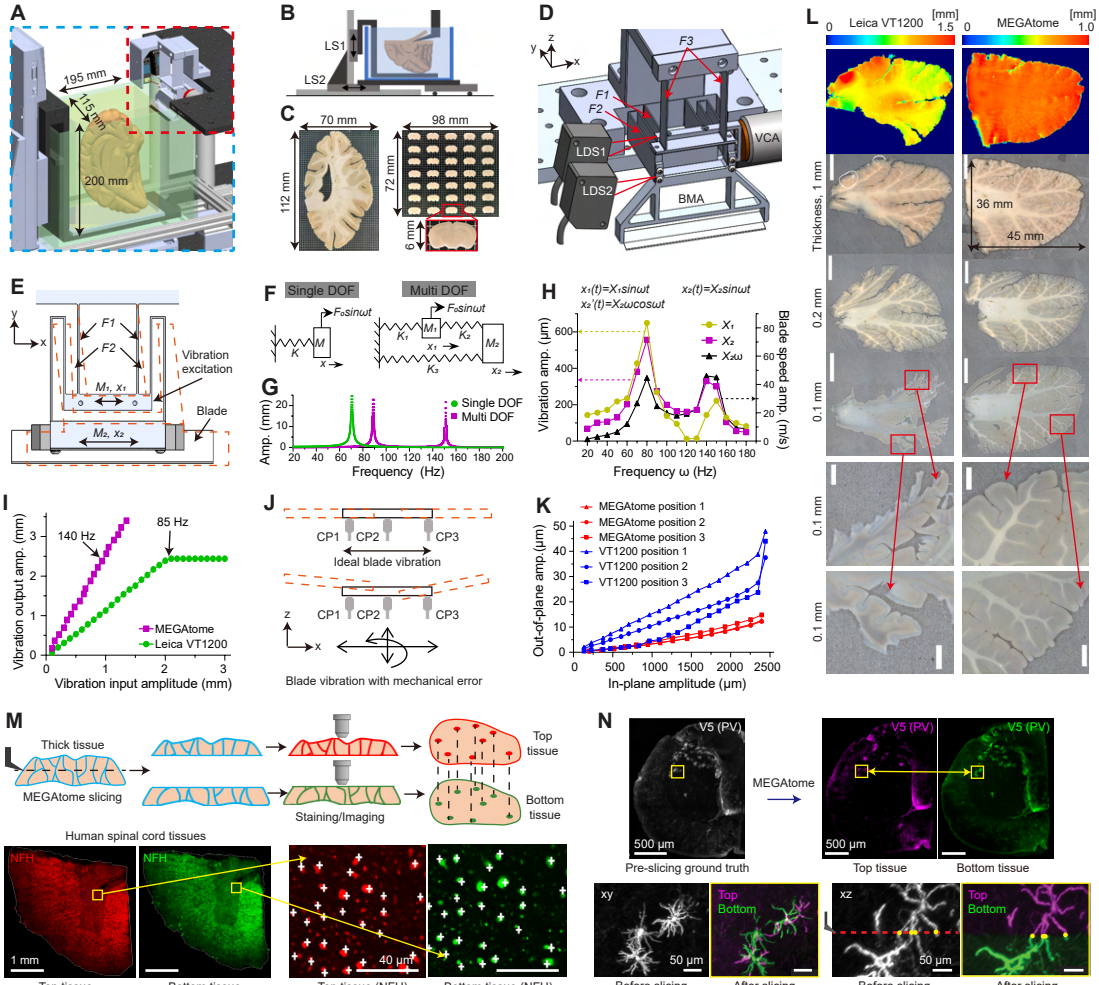
A
195 mm
115 mm
200 mm
B
LS1
LS2
C
70 mm
98 mm
112 mm
72 mm
6 mm
D
F3
F1
F2
LDS1
LDS2
VCA
BMA
E
F1
F2
Vibration excitation
Blade
F
Single DOF
Multi DOF
G
Single DOF
Multi DOF
Amp. (mm)
Frequency (Hz)
H
Vibration amp. (μm)
Blade speed amp. (m/s)
Frequency ω (Hz)
I
140 Hz
85 Hz
MEGAtome
Leica VT1200
Vibration output amp. (mm)
Vibration input amplitude (mm)
J
CP1
CP2
CP3
Ideal blade vibration
Blade vibration with mechanical error
K
MEGAtome position 1
MEGAtome position 2
MEGAtome position 3
VT1200 position 1
VT1200 position 2
VT1200 position 3
Out-of-plane amp.(μm)
In-plane amplitude (μm)
L
Leica VT1200
MEGAtome
Thickness, 1 mm
0.2 mm
0.1 mm
36 mm
45 mm
M
Thick tissue
MEGAtome slicing
Staining/Imaging
Top tissue
Bottom tissue
Human spinal cord tissues
NFH
1 mm
40 μm
Top tissue
Bottom tissue
Top tissue (NFH)
Bottom tissue (NFH)
N
V5 (PV)
MEGAtome
500 μm
Pre-slicing ground truth
Top tissue
Bottom tissue
xy
xz
Top
Bottom
50 μm
Before slicing
After slicing

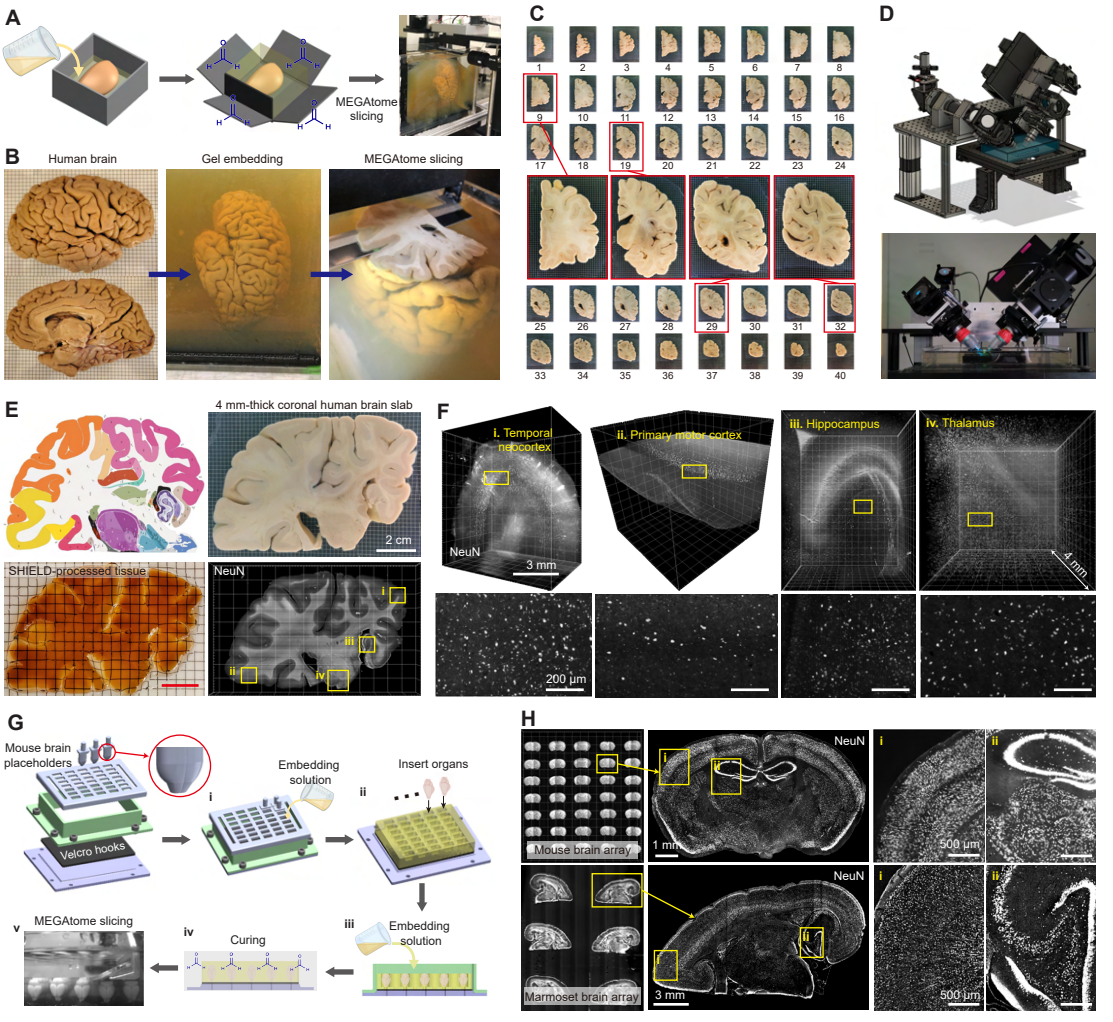
A
MEGAtome slicing
B
Human brain
Gel embedding
MEGAtome slicing
C
D
E
4 mm-thick coronal human brain slab
2 cm
SHIELD-processed tissue
NeuN
F
i. Temporal neocortex
ii. Primary motor cortex
iii. Hippocampus
iv. Thalamus
NeuN
3 mm
4 mm
200 µm
G
Mouse brain placeholders
Velcro hooks
Embedding solution
Insert organs
Embedding solution
Curing
MEGAtome slicing
H
NeuN
Mouse brain array
1 mm
500 µm
Marmoset brain array
3 mm

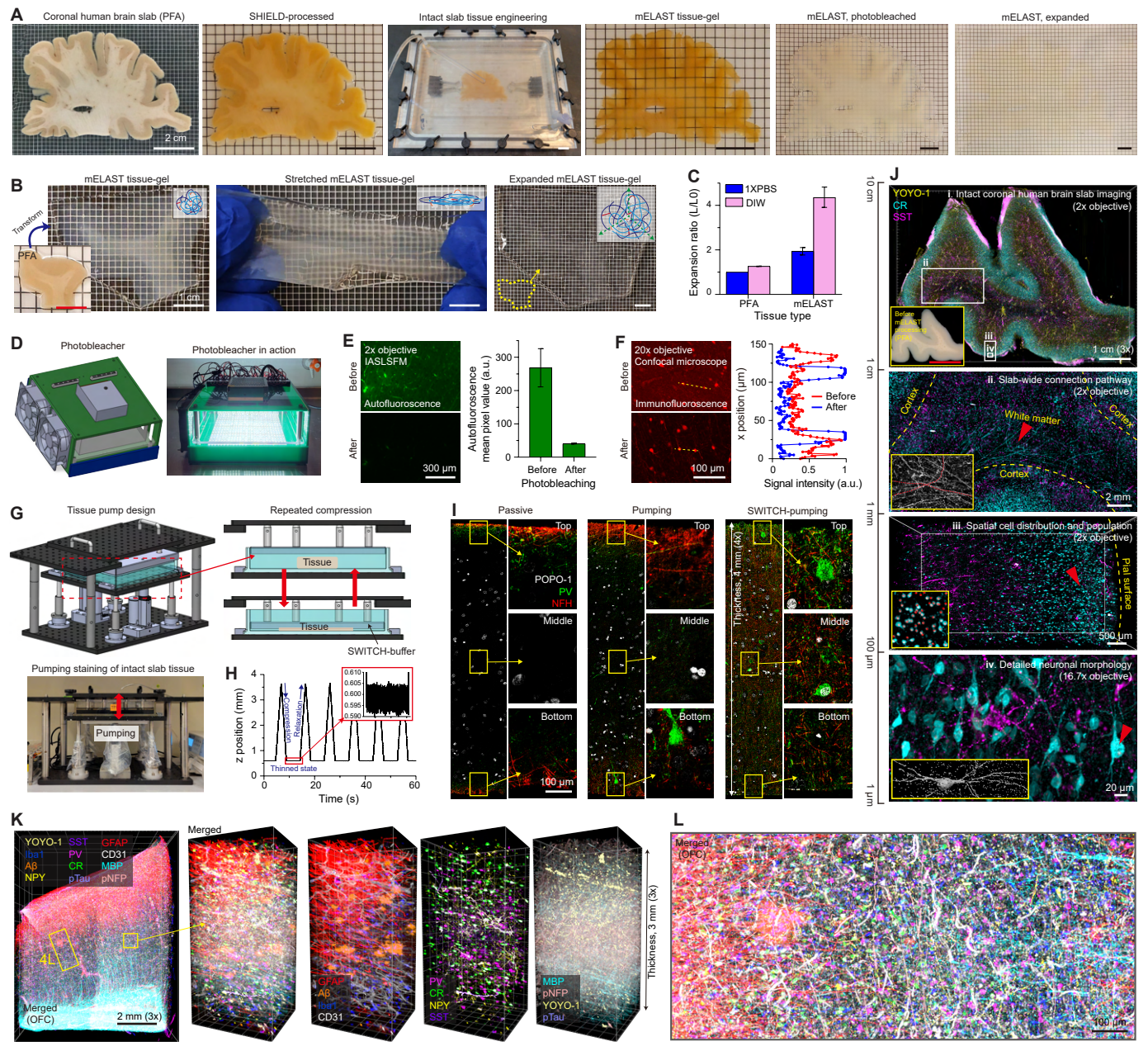
A
Coronal human brain slab (PFA)
SHIELD-processed
Intact slab tissue engineering
mELAST tissue-gel
mELAST, photobleached
mELAST, expanded
2 cm
B
mELAST tissue-gel
Stretched mELAST tissue-gel
Expanded mELAST tissue-gel
Transform
PFA
1 cm
C
1XPBS
DIW
Expansion ratio (L/L0)
PFA
mELAST
Tissue type
D
Photobleacher
Photobleacher in action
E
2x objective
IASLSFM
Before
Autofluorescence
After
300 μm
Autofluorescence
mean pixel value (a.u.)
Before
After
Photobleaching
F
20x objective
Confocal microscope
Before
Immunofluorescence
After
100 μm
x position (μm)
Before
After
Signal intensity (a.u.)
G
Tissue pump design
Repeated compression
Tissue
Tissue
SWITCH-buffer
Pumping staining of intact slab tissue
Pumping
H
z position (mm)
Compression
Relaxation
Thinned state
Time (s)
I
Passive
Pumping
SWITCH-pumping
Top
Middle
Bottom
POPO-1
PV
NFH
Thickness, 4 mm (4x)
100 μm
J
YOYO-1
CR
SST
i. Intact coronal human brain slab imaging
(2x objective)
ii
iii
iv
1 cm (3x)
ii. Slab-wide connection pathway
(2x objective)
Cortex
White matter
Cortex
Cortex
2 mm
iii. Spatial cell distribution and population
(2x objective)
Pial surface
500 μm
iv. Detailed neuronal morphology
(16.7x objective)
20 μm
10 cm
1 cm
1 mm
100 μm
1 μm
K
YOYO-1
SST
GFAP
Iba1
PV
CD31
Aβ
CR
MBP
NPY
pTau
pNFP
4L
Merged
(OFC)
2 mm (3x)
Merged
GFAP
Aβ
CD31
PV
CR
NPY
SST
MBP
pNFP
YOYO-1
pTau
Thickness, 3 mm (3x)
L
Merged
(OFC)
100 μm

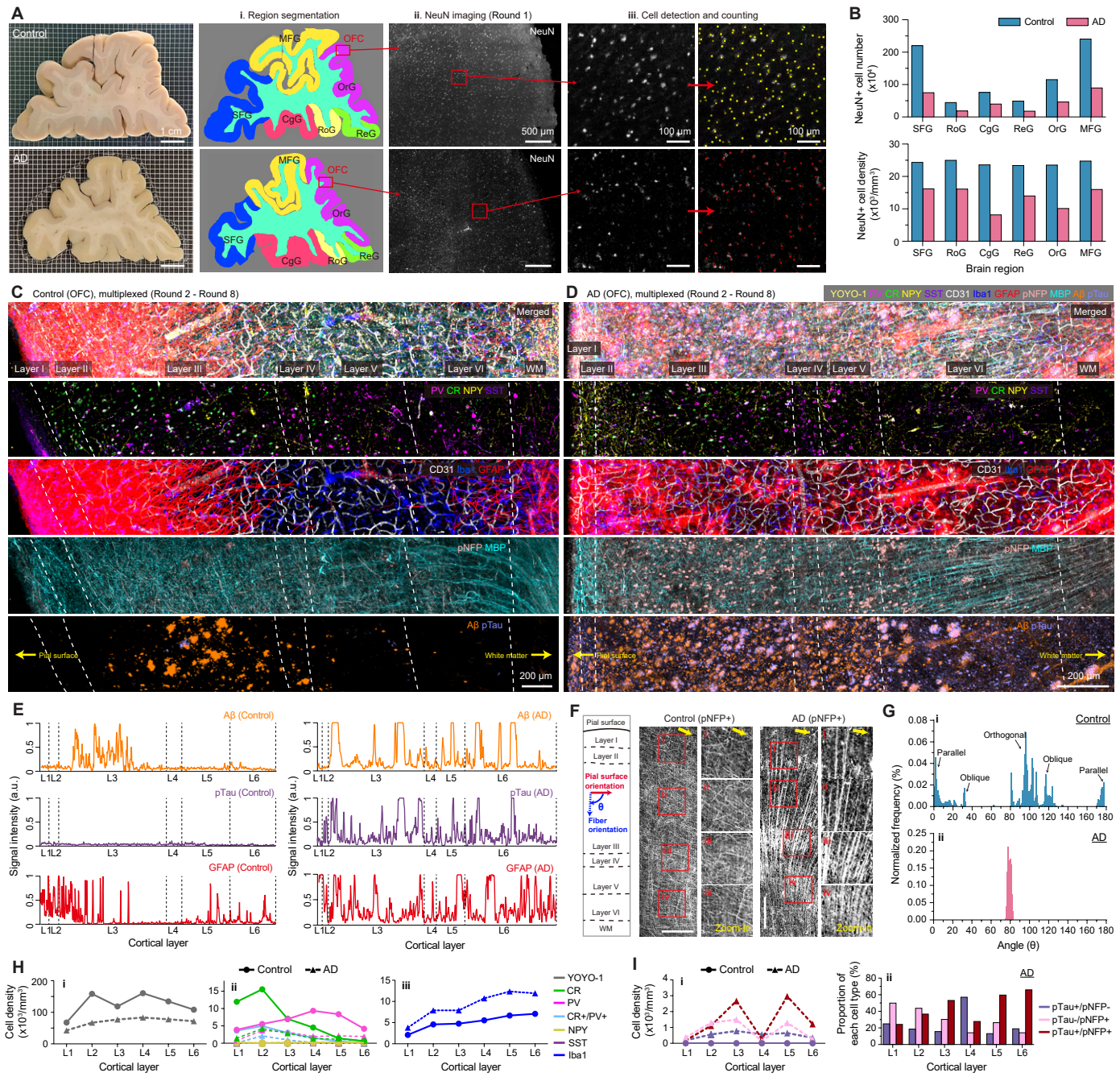
A
i. Region segmentation
ii. NeuN imaging (Round 1)
iii. Cell detection and counting
Control
AD
MFG
OFC
OrG
SFG
CgG
RoG
ReG
NeuN
1 cm
500 μm
100 μm
B
Control
AD
NeuN+ cell number (x10⁴)
NeuN+ cell density (x10³/mm³)
SFG
RoG
CgG
ReG
OrG
MFG
Brain region
C
Control (OFC), multiplexed (Round 2 - Round 8)
D
AD (OFC), multiplexed (Round 2 - Round 8)
YOYO-1 PV CR NPY SST CD31 Iba1 GFAP pNFP MBP Aβ pTau
Merged
Layer I
Layer II
Layer III
Layer IV
Layer V
Layer VI
WM
PV CR NPY SST
CD31 Iba1 GFAP
pNFP MBP
Aβ pTau
Pial surface
White matter
200 μm
E
Aβ (Control)
Aβ (AD)
pTau (Control)
pTau (AD)
GFAP (Control)
GFAP (AD)
Signal intensity (a.u.)
Cortical layer
F
Pial surface
Layer I
Layer II
Pial surface orientation
θ
Fiber orientation
Layer III
Layer IV
Layer V
Layer VI
WM
Control (pNFP+)
AD (pNFP+)
Zoom-in
G
i
Control
Orthogonal
Parallel
Oblique
ii
AD
Normalized frequency (%)
Angle (θ)
H
Control
AD
Cell density (x10³/mm³)
Cortical layer
YOYO-1
CR
PV
CR+/PV+
NPY
SST
Iba1
I
Proportion of each cell type (%)
pTau+/pNFP-
pTau-/pNFP+
pTau+/pNFP+

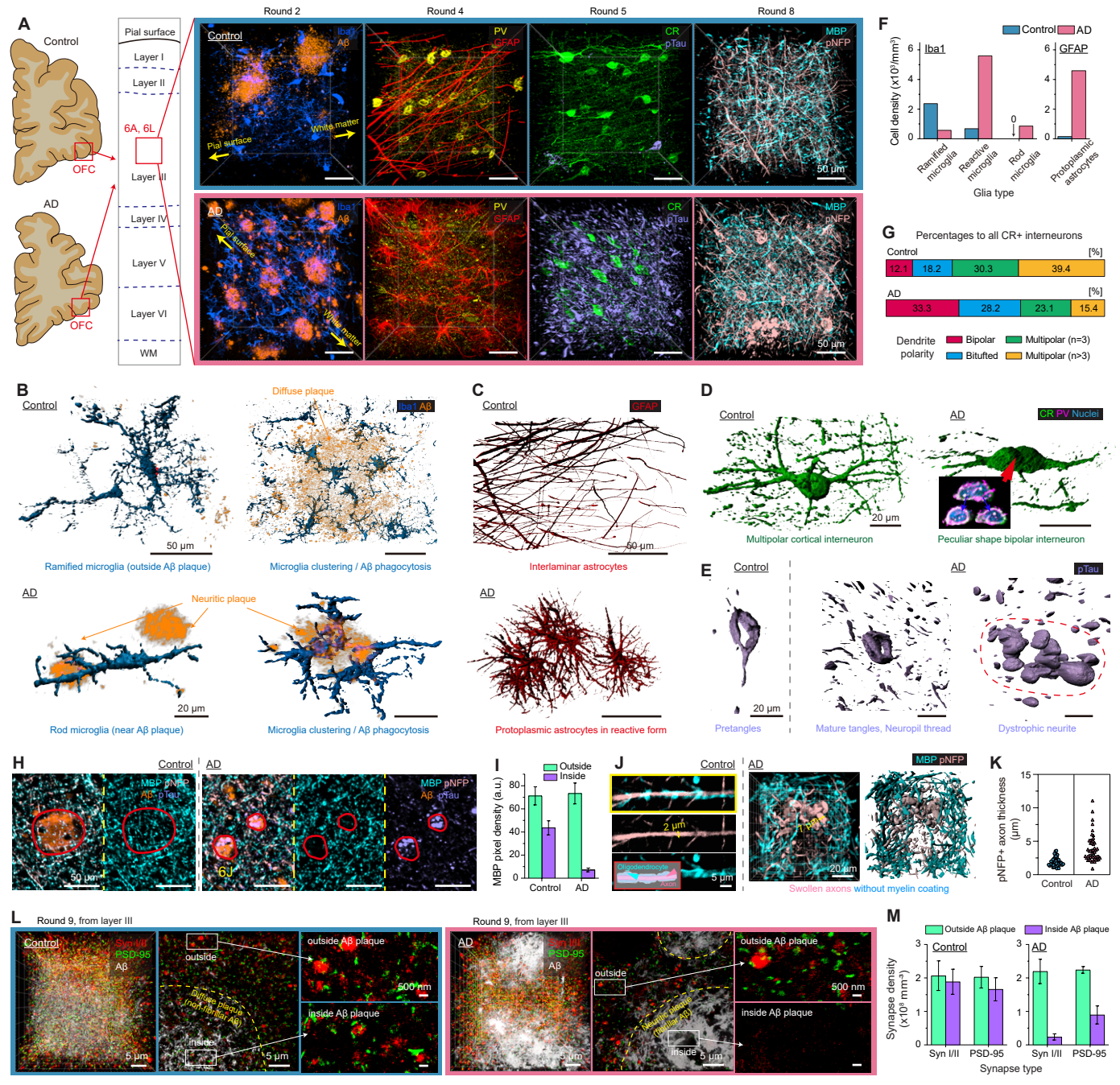
A
Control
AD
OFC
Pial surface
Layer I
Layer II
6A, 6L
Layer III
Layer IV
Layer V
Layer VI
WM
Round 2
Round 4
Round 5
Round 8
Iba1
Aβ
PV
GFAP
CR
pTau
MBP
pNFP
White matter
50 µm
F
Control
AD
Iba1
GFAP
Cell density (x10³/mm²)
Ramified microglia
Reactive microglia
Rod microglia
Protoplasmic astrocytes
Glia type
G
Percentages to all CR+ interneurons
Control
[%]
12.1
18.2
30.3
39.4
AD
33.3
28.2
23.1
15.4
Dendrite polarity
Bipolar
Bitufted
Multipolar (n=3)
Multipolar (n>3)
B
Diffuse plaque
Ramified microglia (outside Aβ plaque)
Microglia clustering / Aβ phagocytosis
Neuritic plaque
Rod microglia (near Aβ plaque)
C
GFAP
Interlaminar astrocytes
Protoplasmic astrocytes in reactive form
D
CR PV Nuclei
20 µm
Multipolar cortical interneuron
Peculiar shape bipolar interneuron
E
pTau
Pretangles
Mature tangles, Neuropil thread
Dystrophic neurite
H
MBP pNFP
Aβ pTau
6J
I
Outside
Inside
MBP pixel density (a.u.)
J
2 µm
Oligodendrocyte
Axon
Swollen axons without myelin coating
K
pNFP+ axon thickness (µm)
L
Round 9, from layer III
Syn I/II
PSD-95
outside
inside
Diffuse plaque (non-fibrillar Aβ)
Neuritic plaque (fibrillar Aβ)
outside Aβ plaque
inside Aβ plaque
500 nm
M
Outside Aβ plaque
Inside Aβ plaque
Synapse density (x10¹⁰ mm⁻³)
Synapse type

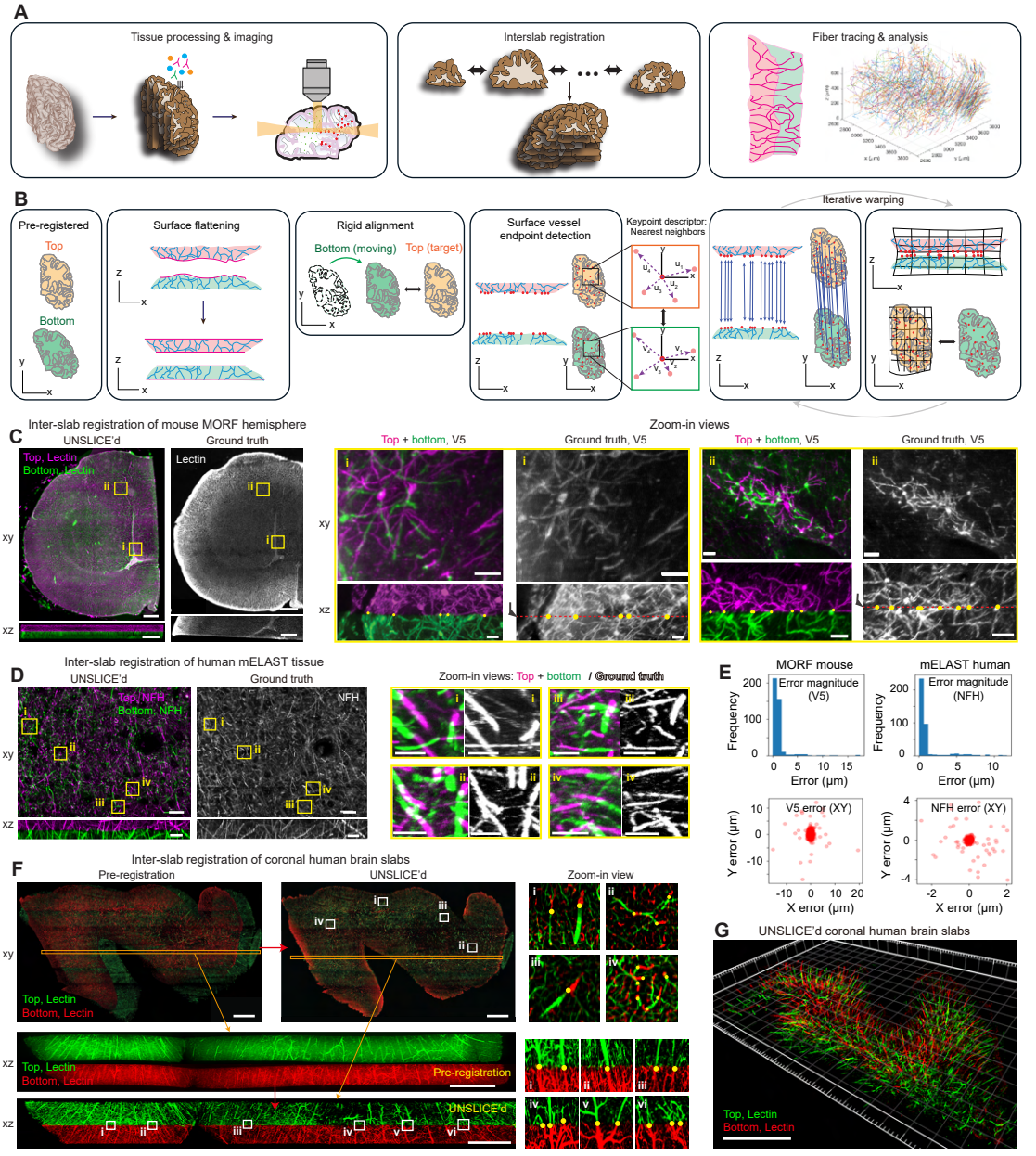
A
Tissue processing & imaging
Interslab registration
Fiber tracing & analysis
B
Pre-registered
Top
Bottom
Surface flattening
Rigid alignment
Bottom (moving)
Top (target)
Surface vessel endpoint detection
Keypoint descriptor: Nearest neighbors
Iterative warping
C
Inter-slab registration of mouse MORF hemisphere
UNSLICE'd
Ground truth
Top, Lectin
Bottom, Lectin
Lectin
Zoom-in views
Top + bottom, V5
Ground truth, V5
xy
xz
D
Inter-slab registration of human mELAST tissue
UNSLICE'd
Ground truth
Top, NFH
Bottom, NFH
NFH
Zoom-in views: Top + bottom / Ground truth
E
MORF mouse
mELAST human
Error magnitude (V5)
Error magnitude (NFH)
Frequency
Error (µm)
V5 error (XY)
NFH error (XY)
Y error (µm)
X error (µm)
F
Inter-slab registration of coronal human brain slabs
Pre-registration
UNSLICE'd
Zoom-in view
Top, Lectin
Bottom, Lectin
G
UNSLICE'd coronal human brain slabs
Top, Lectin
Bottom, Lectin

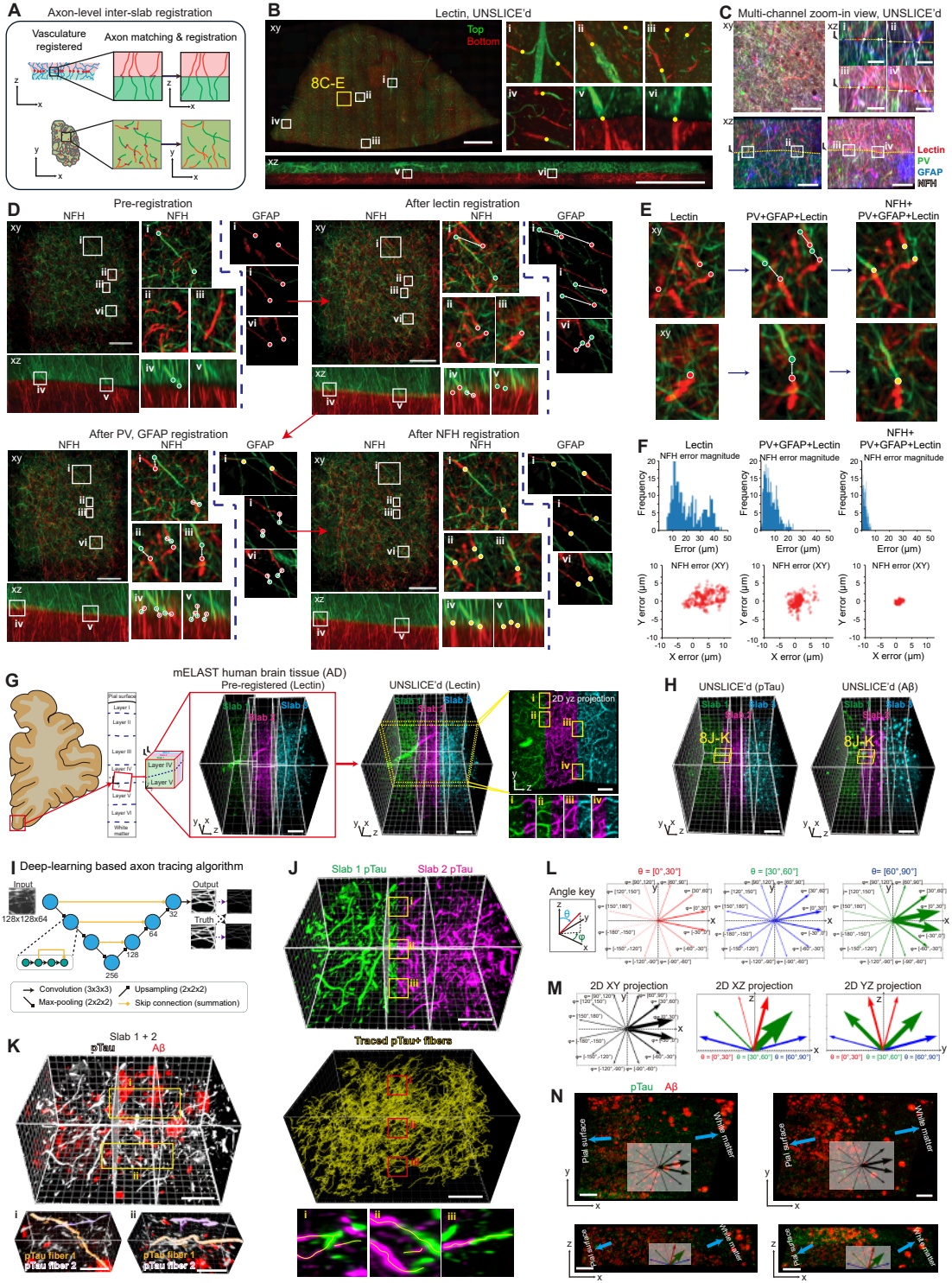
A
Axon-level inter-slab registration
Vasculature registered
Axon matching & registration
B
Lectin, UNSLICE'd
Top
Bottom
8C-E
C
Multi-channel zoom-in view, UNSLICE'd
Lectin
PV
GFAP
NFH
D
Pre-registration
After lectin registration
After PV, GFAP registration
After NFH registration
E
Lectin
PV+GFAP+Lectin
NFH+ PV+GFAP+Lectin
F
NFH error magnitude
Frequency
Error (μm)
NFH error (XY)
Y error (μm)
X error (μm)
G
mELAST human brain tissue (AD)
Pre-registered (Lectin)
UNSLICE'd (Lectin)
2D yz projection
Pial surface
Layer I
Layer II
Layer III
Layer IV
Layer V
Layer VI
White matter
H
UNSLICE'd (pTau)
UNSLICE'd (Aβ)
8J-K
I
Deep-learning based axon tracing algorithm
Input
Output
Truth
128x128x64
32
64
128
256
Convolution (3x3x3)
Upsampling (2x2x2)
Max-pooling (2x2x2)
Skip connection (summation)
J
Slab 1 pTau
Slab 2 pTau
Traced pTau+ fibers
K
Slab 1 + 2
pTau
Aβ
pTau fiber 1
pTau fiber 2
L
Angle key
θ = [0°,30°]
θ = [30°,60°]
θ= [60°,90°]
M
2D XY projection
2D XZ projection
2D YZ projection
N
pTau
Aβ
Pial surface
White matter